

Spatial Resolution Properties of Motion-Compensated Tomographic Image Reconstruction Methods

Se Young Chun*, *Member, IEEE*, and Jeffrey A. Fessler, *Fellow, IEEE*

Abstract—Many motion-compensated image reconstruction (MCIR) methods have been proposed to correct for subject motion in medical imaging. MCIR methods incorporate motion models to improve image quality by reducing motion artifacts and noise. This paper analyzes the spatial resolution properties of MCIR methods and shows that nonrigid local motion can lead to nonuniform and anisotropic spatial resolution for conventional quadratic regularizers. This undesirable property is akin to the known effects of interactions between heteroscedastic log-likelihoods (e.g., Poisson likelihood) and quadratic regularizers. This effect may lead to quantification errors in small or narrow structures (such as small lesions or rings) of reconstructed images. This paper proposes novel spatial regularization design methods for three different MCIR methods that account for known nonrigid motion. We develop MCIR regularization designs that provide approximately uniform and isotropic spatial resolution and that match a user-specified target spatial resolution. Two-dimensional PET simulations demonstrate the performance and benefits of the proposed spatial regularization design methods.

Index Terms—Isotropic and uniform spatial resolution, motion-compensated image reconstruction, nonrigid motion, quadratic regularization, regularization design.

I. INTRODUCTION

MOTION can degrade image quality in medical imaging. Often, medical imaging systems cannot capture ideal quality images due to their innate acquisition speeds and patient motion. Gating methods have been investigated to reduce motion artifacts [1], [2], but can suffer from insufficient measurements that result in low signal-to-noise ratio (SNR) images. Motion-compensated image reconstruction (MCIR) methods have been studied for various imaging modalities to improve image quality by using all collected data and motion information so that high SNR images are reconstructed without motion artifacts [3]–[16].

MCIR methods differ in terms of how they incorporate motion information. We focus here on three common MCIR methods: post-reconstruction motion correction (PMC) [3]–[5],

Manuscript received February 08, 2012; revised March 14, 2012; accepted March 20, 2012. Date of publication April 03, 2012; date of current version June 26, 2012. This work was supported in part by the National Institutes of Health/National Cancer Institute (NIH/NCI) under Grant 1P01 CA87634. *Asterisk indicates corresponding author.*

*S. Y. Chun is with the Departments of Engineering and Computer Science and Radiology, University of Michigan, Ann Arbor, MI 48109 USA (e-mail: delight@umich.edu).

J. A. Fessler is with the Department of Engineering and Computer Science, University of Michigan, Ann Arbor, MI 48109 USA (e-mail: fessler@umich.edu).

Color versions of one or more of the figures in this paper are available online at <http://ieeexplore.ieee.org>.

Digital Object Identifier 10.1109/TMI.2012.2192133

TABLE I
ACRONYMS

Acronym	
MCIR	motion-compensated image reconstruction
LIR	local impulse response
Acronym	Reconstruction method
SGR	single gated reconstruction
PMC	post-reconstruction motion correction
MTR	motion-compensated temporal regularization
PMM	the parametric motion model
Acronym	Regularization method
-S	standard quadratic regularizer
-C	certainty-based regularizer
-P	proposed regularizer

motion-compensated temporal regularization (MTR) [6], [7], and the parametric motion model (PMM) [8]–[16] (see Table I). These models have also been used in non-medical super-resolution applications [17]–[20]. These MCIR methods have shown promising results for reducing noise and motion artifacts. MCIR methods have great potential for improving image quality and benefiting the tasks used in medical imaging (e.g., better quantitative accuracy for PET or lower radiation dose for CT).

The interactions between heteroscedastic log-likelihood models (e.g., Poisson measurements) and conventional static quadratic regularizers lead to nonuniform and anisotropic spatial resolution [21]. In this paper, we show analytically that these undesired properties can become worse in regularized MCIR methods due to local motion, may cause nonuniform and anisotropic spatial resolution, and produce quantification errors in small or narrow structures such as small lesions or rings of reconstructed images. For example, Fig. 1 shows the contours of local impulse response (LIR) functions of Target (desired LIR), SGR-S (single gated reconstruction with conventional spatial regularizer using one frame), and PMC-S (PMC with conventional static spatial regularizer using four frames) in a 2-D PET simulation (see Table I for acronyms). Each LIR was generated by subtracting the reconstructed image of the noiseless projection data of the original image from the reconstructed image of the noiseless projection of the original image with a Kronecker impulse at one point. The Target has isotropic contours, but SGR-S has a skewed LIR due to the interaction between the log-likelihood and the quadratic regularizer. This skewness became worse for the LIR of PMC-S due to affine motion between image frames.

There have been many studies of the spatial resolution properties of static image reconstruction [21]–[27] and dynamic image reconstruction [28]. Regularizers that provide nearly uniform spatial resolution, or “certainty-based” regularizers, have been

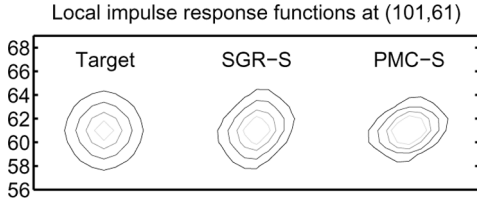


Fig. 1. Contours of LIRs: Target, SGR-S (single gate), PMC-S (four gates with motion). Incorporated motion information may introduce additional nonuniform and anisotropic spatial resolution to the static case.

proposed for quadratic regularization with PET [21], fully 3-D PET [23], and for nonquadratic regularizers with PET [26]. Regularizers that achieve approximately uniform and isotropic spatial resolution have been developed for PET [24], [25] and 2-D fan-beam CT [27]. However, there has been little such research for regularized MCIR methods.

This paper investigates the spatial resolution properties of three popular MCIR methods (PMC, PMM, and MTR). Based on this analysis, we propose quadratic regularizers that can achieve approximately isotropic and uniform spatial resolution even in the presence of nonrigid motion and for heteroscedastic log-likelihoods. For regularizer design, we extend the “analytical approach” [27], [29] to MCIR methods [30] for the case of known nonrigid motion. The known motion assumption can be suitable for some multimodal medical imaging applications such as PET-CT [9], [10], [12] and PET-MR systems [16].

This paper is organized as follows. Section II presents measurement and motion/warp models for MCIR methods. Section III introduces three different MCIR methods and their LIRs. Section IV investigates how to design spatial regularizers for MCIR methods that provide approximately uniform and isotropic spatial resolution for nonrigid motion by extending analytical approach. Section V illustrates the proposed spatial regularizers by 2-D PET simulations with nonrigid motion.

II. MCIR MODELS

A. Measurement Model

Most medical imaging systems cannot capture an entire dataset instantaneously, but rather record a sequence of measurements over some time interval. For example, X-ray CT scanners acquire about 1000 projection views during a sub-second rotation around the object. MCIR methods are needed when the time-varying object $f(\vec{x}, t)$ has non-negligible motion during such an acquisition interval. Often one can use gating or temporal binning to group the measurements into M sets, called “frames” here, such that object motion is negligible *within* each frame, and then one can focus on the object motion *between* frames. This type of discrete approximation to continuous object motion is ubiquitous in MCIR models and we adopt it here as well. Let \mathbf{y}_m denote the vector of measurements associated with the m th frame, e.g., a frame in a gated scan. We assume the time-varying object $f(\vec{x}, t)$ is approximately motionless during the acquisition of each \mathbf{y}_m . Let t_m denote the time associated with the m th frame, and let $\mathbf{f}_m = (f(\vec{x}_1, t_m), \dots, f(\vec{x}_N, t_m))$ denote a spatial discretization of the object $f(\cdot, t_m)$ where \vec{x}_j denotes the center of the j th voxel for $j = 1, \dots, N$, and N de-

notes the number of voxels. We assume that the measurements are related to the object linearly as follows:

$$\mathbf{y}_m = \mathbf{A}_m \mathbf{f}_m + \boldsymbol{\epsilon}_m, \quad m = 1, \dots, M \quad (1)$$

where \mathbf{A}_m denotes the system model for the m th frame, $\boldsymbol{\epsilon}_m$ denotes noise, and M is the number of gates or frames. We allow the system model \mathbf{A}_m to possibly differ for each frame to accommodate systems that rotate such as gated SPECT or CT or that can otherwise change sampling properties dynamically such as MRI. In some cases, we assume that $\mathbf{A}_m = \mathbf{D}_m \mathbf{A}_0, \forall m$ where \mathbf{D}_m is a diagonal matrix (e.g., PET scan, gated MRI scan with fixed k-space sampling, or a video sequence).

B. Basic Warp Model

For a given spatial transformation $T_{m,n} : \mathbb{R}^d \rightarrow \mathbb{R}^d$, we can define a warp operator $\mathcal{T}_{m,n}$ as follows:

$$f(\vec{x}, t_m) = (\mathcal{T}_{m,n} f)(\vec{x}, t_n) \triangleq f(T_{m,n}(\vec{x}), t_n) \quad (2)$$

where \vec{x} belongs to an image domain \mathbb{R}^d at time t_m and d is usually 2 or 3. We can discretize the warp $\mathcal{T}_{m,n}$ to define a map from the image \mathbf{f}_n to the image \mathbf{f}_m as follows:

$$\mathbf{f}_m = \mathbf{T}_{m,n} \mathbf{f}_n, \quad n, m = 1, \dots, M. \quad (3)$$

For applications with periodic motion, we can additionally define $\mathbf{f}_{M+1} \triangleq \mathbf{f}_1$ and $\mathbf{T}_{M+1,M} \triangleq \mathbf{T}_{1,M}$. The $N \times N$ matrix $\mathbf{T}_{m,n}$ can be implemented with any interpolation method; we used a B-spline based image warp [31] for our empirical results. Let $|\nabla T_{m,n}(\vec{x})|$ denote the determinant of the Jacobian matrix of a transform $T_{m,n}(\vec{x})$ for a warp $\mathbf{T}_{m,n}$. Throughout, we assume the warps $\mathbf{T}_{m,n}$ (or equivalently $T_{m,n}$ or $\mathcal{T}_{m,n}$) are known.

C. Total Activity-Preserving Warp Model

In many medical imaging applications, total activity (or total mass) is preserved during the scan [32], [33] and this property has been used in some MCIR methods [34]. To enforce this constraint, the operator $\mathcal{T}_{m,n}$ must not change the total activity of an image. To preserve total activity (or mass), one can define a modification of the operator $\mathcal{T}_{m,n}$ that uses the Jacobian determinant of $T_{m,n}$

$$f(\vec{x}, t_m) = (\tilde{\mathcal{T}}_{m,n} f)(\vec{x}, t_n) \triangleq |\nabla T_{m,n}(\vec{x})|^p f(T_{m,n}(\vec{x}), t_n) \quad (4)$$

where $p = 1$. To verify that total activity is preserved, note that

$$\begin{aligned} \int_{\mathbb{R}^d} f(\vec{x}, t_m) d\vec{x} &= \int_{\mathbb{R}^d} |\nabla T_{m,n}(\vec{x})| f(T_{m,n}(\vec{x}), t_n) d\vec{x} \\ &= \int_{\mathbb{R}^d} f(\vec{y}, t_n) d\vec{y} \end{aligned} \quad (5)$$

where $\vec{y} = T_{m,n}(\vec{x})$. Similarly, we can define a discrete-space warp corresponding to (4) that approximately preserves total activity

$$\mathbf{f}_m = \tilde{\mathbf{T}}_{m,n} \mathbf{f}_n, \quad n, m = 1, \dots, M \quad (6)$$

where

$$\mathring{\mathbf{T}}_{m,n} \triangleq \mathbf{D}(|\nabla T_{m,n}(\vec{x}_j)|^p) \mathbf{T}_{m,n} \quad (7)$$

and $\mathbf{D}(|\nabla T_{m,n}(\vec{x}_j)|^p)$ is a $N \times N$ diagonal matrix with elements $\{|\nabla T_{m,n}(\vec{x}_j)|^p\}$, $j = 1, \dots, N$ and $p = 1$. We use (4) and (6) for the analyses in this paper, but one can simply let $p = 0$ if a total activity-preserving model is not needed.

The warp operator $\mathcal{T}_{m,n}$ in (2) acts pointwise, so its discretized version in (3) also acts approximately pointwise. Therefore, the diagonal matrix in (7) that is applied to the left-hand side of $\mathbf{T}_{m,n}$ can be replaced (approximately) by a closely related diagonal matrix on the right-hand side of $\mathbf{T}_{m,n}$ by simply adjusting the spatial coordinates as follows:

$$\begin{aligned} \mathbf{D}(|\nabla T_{m,n}(\vec{x}_j)|^p) \mathbf{T}_{m,n} &\approx \mathbf{T}_{m,n} \mathbf{D}(|\nabla T_{m,n}(T_{n,m}(\vec{x}_j))|^p) \\ &\approx \mathbf{T}_{m,n} \mathbf{D}(|\nabla T_{n,m}(\vec{x}_j)|^{-p}) \end{aligned} \quad (8)$$

where $|\nabla T_{m,n}(T_{n,m}(\vec{x}_j))| |\nabla T_{n,m}(\vec{x}_j)| = 1$ by the chain rule.

In some cases, we assume that invertibility, symmetry, and transitivity properties hold for $\mathring{\mathbf{T}}_{m,n}$, i.e.,

$$|\nabla T_{m,n}| > 0, \quad \forall n, m, \quad (9)$$

$$\mathring{\mathbf{T}}_{m,n}^{-1} = \mathring{\mathbf{T}}_{n,m}, \quad \forall n, m, \quad (10)$$

$$\mathring{\mathbf{T}}_{m,n} = \mathring{\mathbf{T}}_{m,m-1} \cdots \mathring{\mathbf{T}}_{n+1,n}, \quad \forall m > n. \quad (11)$$

These assumptions are reasonable for usual patient motion such as respiratory or cardiac motion. In practice, one can estimate motion models that satisfy these conditions [35], [36].

III. LOCAL IMPULSE RESPONSE FOR MCIR

We consider three MCIR methods: PMC [3]–[5], PMM [8]–[14], [17], [19], and MTR [6], [7], [20], [37]. Here, we treat the nonrigid motion information as predetermined (known). In this section, we derive the LIRs for regularized versions of these MCIR methods.

A. Single Gated Reconstruction (SGR)

Often one can reconstruct each image $\hat{\mathbf{f}}_m$ from the corresponding measurement \mathbf{y}_m based on the model (1) and some prior knowledge (e.g., a smoothness prior). A single gated (frame) reconstruction (SGR) can be obtained as follows:

$$\hat{\mathbf{f}}_m \triangleq \underset{\mathbf{f}_m}{\operatorname{argmin}} L(\mathbf{y}_m, \mathbf{A}_m \mathbf{f}_m) + \eta R(\mathbf{f}_m) \quad (12)$$

where L is a likelihood function derived from (1), R is a spatial regularizer, and η is a spatial regularization parameter.

For any single-frame estimator $\hat{\mathbf{f}}_m(\mathbf{y}_m)$, one can define the LIR for the j th pixel as

$$l_m^j \triangleq \lim_{\delta \rightarrow 0} \frac{\hat{\mathbf{f}}_m(\bar{\mathbf{y}}_m(\mathbf{f}_m + \delta \mathbf{e}_j)) - \hat{\mathbf{f}}_m(\bar{\mathbf{y}}_m(\mathbf{f}_m))}{\delta} \quad (13)$$

where $\bar{\mathbf{y}}_m$ is the mean of \mathbf{y}_m and \mathbf{e}_j is a unit vector with one at the j th element. If L in (12) is a negative Poisson log-likelihood

function (i.e., $L(\mathbf{y}, \mathbf{u}) \triangleq \sum_i [\mathbf{u}]_i - [\mathbf{y}]_i \log[\mathbf{u}]_i$), then one can show that the LIR in (13) can be approximated [21]

$$\begin{aligned} l_m^j &\approx [\mathbf{A}'_m \mathbf{W}_m \mathbf{A}_m + \eta \mathbf{R}_m]^{-1} \mathbf{A}'_m \mathbf{W}_m \mathbf{A}_m \mathbf{e}_j \\ &\approx [\mathbf{F}_m + \eta \mathbf{R}_m]^{-1} \mathbf{F}_m \mathbf{e}_j \end{aligned} \quad (14)$$

where $\mathbf{W}_m \triangleq \mathbf{D}(1/[\bar{\mathbf{y}}_m(\mathbf{f}_m)]_i)$ is a diagonal matrix, the Hessian of the regularizer is $\mathbf{R}_m \triangleq \nabla^2 R(\hat{\mathbf{f}}_m)$, $\hat{\mathbf{f}}_m = \hat{\mathbf{f}}_m(\bar{\mathbf{y}}_m(\mathbf{f}_m))$, “ \prime ” denotes matrix transpose, and the Fisher information matrix is

$$\mathbf{F}_m \triangleq \mathbf{A}'_m \mathbf{W}_m \mathbf{A}_m.$$

Equation (14) implies that the LIR of (1) for a Poisson likelihood can be approximated with the LIR of (1) for a penalized weighted least square (PWLS) likelihood. Thus, the analysis in the paper also applies to any PWLS model. Sometimes, a regularizer depends on the noiseless projection $\bar{\mathbf{y}}_m(\mathbf{f}_m)$, which is unavailable. However, as shown in [21], a *plug-in* approach that replaces $\bar{\mathbf{y}}_m(\mathbf{f}_m)$ by \mathbf{y}_m (or smoothed \mathbf{y}_m) works well for the regularization design since \mathbf{A}_m contains a blurring operator. In the simulation, we will show that this is also the case for MCIRs.

B. Postreconstruction Motion Correction (PMC)

Once the frames $\hat{\mathbf{f}}_1, \dots, \hat{\mathbf{f}}_M$ are reconstructed individually from (12) for all m , one way to improve the SNR would be to average all of them. However, the resulting image would be contaminated by motion blur due to the mismatch between frames. Using the motion information to map each image \mathbf{f}_m to a single image’s coordinates can reduce motion artifacts. Without loss of generality, we chose \mathbf{f}_1 as our reference image. Using (6) and (12), a natural definition for the PMC estimator is the following motion-compensated average:

$$\hat{\mathbf{f}}_{\text{PMC}} \triangleq \frac{1}{M} \sum_{m=1}^M \mathring{\mathbf{T}}_{1,m} \hat{\mathbf{f}}_m. \quad (15)$$

Using (14), (10), and (6), one can derive the LIR for the PMC estimator (15) at the j th pixel of the first frame as follows:

$$\begin{aligned} l_{\text{PMC}}^j &\approx \frac{1}{M} \sum_{m=1}^M \mathring{\mathbf{T}}_{1,m} [\mathbf{F}_m + \eta \mathbf{R}_m]^{-1} \mathbf{F}_m \mathring{\mathbf{T}}_{m,1} \mathbf{e}_j \\ &\approx \frac{1}{M} \sum_{m=1}^M [\mathring{\mathbf{F}}_m + \eta \mathring{\mathbf{R}}_m]^{-1} \mathring{\mathbf{F}}_m \mathbf{e}_j \end{aligned} \quad (16)$$

where $\mathring{\mathbf{F}}_m \triangleq \mathring{\mathbf{T}}_{m,1}' \mathbf{F}_m \mathring{\mathbf{T}}_{m,1}$ and $\mathring{\mathbf{R}}_m \triangleq \mathring{\mathbf{T}}_{m,1}' \mathbf{R}_m \mathring{\mathbf{T}}_{m,1}$. We used $\mathring{\mathbf{T}}_{m,1} \mathbf{e}_j$ instead of \mathbf{e}_j as an impulse for the m th frame, which corresponds to an impulse in the first frame.

C. Parametric Motion Model (PMM)

To derive the LIR of the PMM approach, we first must choose a reference image frame among $\{\mathbf{f}_1, \dots, \mathbf{f}_M\}$. Without loss of generality, we assume that \mathbf{f}_1 is our reference image frame. Then, combining the measurement model (1) with the warp

(6) yields a new measurement model that depends only on the image \mathbf{f}_1 instead of the all images \mathbf{f}_m

$$\mathbf{y}_m = \mathbf{A}_m \mathring{\mathbf{T}}_{m,1} \mathbf{f}_1 + \boldsymbol{\epsilon}_m, \quad m = 1, \dots, M.$$

Stacking up these models yields the overall model

$$\mathbf{y}_c = \mathbf{A}_d \mathring{\mathbf{T}}_c \mathbf{f}_1 + \boldsymbol{\epsilon}_c \quad (17)$$

where the components are each stacked accordingly

$$\begin{aligned} \mathbf{y}_c &\triangleq [\mathbf{y}'_1, \dots, \mathbf{y}'_M]' \\ \mathbf{A}_d &\triangleq \text{diag}\{\mathbf{A}_1, \dots, \mathbf{A}_M\} \\ \mathring{\mathbf{T}}_c &\triangleq [\mathbf{I}, \mathring{\mathbf{T}}'_{2,1}, \dots, \mathring{\mathbf{T}}'_{M,1}]' \\ \boldsymbol{\epsilon}_c &\triangleq [\boldsymbol{\epsilon}'_1, \dots, \boldsymbol{\epsilon}'_M]'. \end{aligned} \quad (18)$$

The PMM estimator for the measurement model (17) with a spatial regularizer is

$$\hat{\mathbf{f}}_{\text{PMM}} \triangleq \underset{\mathbf{f}_1}{\text{argmin}} L(\mathbf{y}_c, \mathbf{A}_d \mathring{\mathbf{T}}_c \mathbf{f}_1) + \eta R(\mathbf{f}_1) \quad (19)$$

where L is a negative likelihood function and R is a spatial regularizer.

For the linear measurement model (17) with a negative Poisson log-likelihood function L , similar to (14), one can approximate the LIR [as defined in (13)] for the PMM estimator (19) at the j th pixel as follows:

$$\mathbf{l}_{\text{PMM}}^j \approx [\mathring{\mathbf{T}}_c' \mathbf{F}_d \mathring{\mathbf{T}}_c + \eta \mathbf{R}_{\text{PMM}}]^{-1} \mathring{\mathbf{T}}_c' \mathbf{F}_d \mathring{\mathbf{T}}_c \mathbf{e}_j \quad (20)$$

where $\mathbf{F}_d \triangleq \mathbf{A}_d' \mathbf{W}_d \mathbf{A}_d = \text{diag}\{\mathbf{F}_1, \dots, \mathbf{F}_M\}$ is a block-diagonal matrix, $\mathbf{W}_d \triangleq \mathbf{D}(1/[\bar{\mathbf{y}}_c(\mathbf{f}_1)]_i)$ is a diagonal matrix, $\bar{\mathbf{y}}_c$ is the mean of \mathbf{y}_c , $\mathbf{R}_{\text{PMM}} \triangleq \nabla^2 R(\hat{\mathbf{f}}_{\text{PMM}})$, and $\hat{\mathbf{f}}_{\text{PMM}} = \hat{\mathbf{f}}_{\text{PMM}}(\bar{\mathbf{y}}_c(\mathbf{f}_1))$. Note that

$$\mathring{\mathbf{T}}_c' \mathbf{F}_d \mathring{\mathbf{T}}_c = \sum_{m=1}^M \mathring{\mathbf{T}}_{m,1}' \mathbf{F}_m \mathring{\mathbf{T}}_{m,1} = \sum_{m=1}^M \mathring{\mathbf{F}}_m. \quad (21)$$

Using (20) and (21), we can rewrite the LIR of the PMM estimator at the j th pixel as

$$\mathbf{l}_{\text{PMM}}^j \approx \left[\sum_{m=1}^M \mathring{\mathbf{F}}_m + \eta \mathbf{R}_{\text{PMM}} \right]^{-1} \sum_{m=1}^M \mathring{\mathbf{F}}_m \mathbf{e}_j. \quad (22)$$

D. Motion-Compensated Temporal Regularization (MTR)

The MTR method incorporates the motion information that matches two adjacent images into a temporal regularization term [6], [7]

$$\|\mathbf{f}_{m+1} - \mathring{\mathbf{T}}_{m+1,m} \mathbf{f}_m\|_2^2 \quad (23)$$

for $m = 1, \dots, M-1$. This penalty is added to the cost function in (12) for all m to define the MTR cost function.

Equations (12) for all m and (23) can be represented in a simpler vector-matrix notation. First, stack up (1) for all m as follows:

$$\mathbf{y}_c = \mathbf{A}_d \mathbf{f}_c + \boldsymbol{\epsilon}_c \quad (24)$$

where $\mathbf{f}_c = [\mathbf{f}'_1, \dots, \mathbf{f}'_M]'$ and $\mathbf{A}_d, \boldsymbol{\epsilon}_c$ were defined in (18). Then, the MTR estimator based on (23), (24), and a spatial regularizer is

$$\hat{\mathbf{f}}_{\text{MTR}} \triangleq \underset{\mathbf{f}_c}{\text{argmin}} L(\mathbf{y}_c, \mathbf{A}_d \mathbf{f}_c) + \eta R(\mathbf{f}_c) + \zeta \|\mathbf{T}_{\text{time}} \mathbf{f}_c\|_2^2 \quad (25)$$

where L is a negative likelihood function from the noise model of (24), R is a spatial regularizer, ζ is a temporal regularization parameter, and the temporal differencing matrix is

$$\mathbf{T}_{\text{time}} \triangleq \begin{bmatrix} -\mathring{\mathbf{T}}_{2,1} & \mathbf{I} & & & \\ & & \ddots & & \\ & & & \ddots & \\ & & & & -\mathring{\mathbf{T}}_{M,M-1} & \mathbf{I} \end{bmatrix}. \quad (26)$$

We may also modify \mathbf{T}_{time} for periodic (or pseudo-periodic) image sequences by adding a row corresponding to the term $\|\mathbf{f}_1 - \mathring{\mathbf{T}}_{1,M} \mathbf{f}_M\|^2$. Note that unlike the PMM method that estimates one frame, MTR estimates all image frames.

For the MTR estimator (25) with a negative Poisson log-likelihood function L , one can derive the LIR of the MTR estimator at the j th pixel as follows:

$$\mathbf{l}_{\text{MTR}}^j \approx [\mathbf{F}_d + \eta \mathbf{R}_d + \zeta \mathbf{R}_{\text{time}}]^{-1} \mathbf{F}_d \mathbf{e}_c^j \quad (27)$$

where $\mathbf{R}_d \triangleq \text{diag}\{\mathbf{R}_1, \dots, \mathbf{R}_M\}$, $\mathbf{R}_{\text{time}} \triangleq \mathbf{T}'_{\text{time}} \mathbf{T}_{\text{time}}$, and we define an impulse vector for all frames at j th voxel of the first frame as

$$\mathbf{e}_c^j \triangleq [\mathbf{e}'_j, (\mathring{\mathbf{T}}_{2,1} \mathbf{e}_j)', \dots, (\mathring{\mathbf{T}}_{M,1} \mathbf{e}_j)']' \quad (28)$$

which is the same as the impulse for the PMC in (16). We can interpret the LIR of MTR (27) as follows. For $\zeta = 0$, the LIR of MTR at the j th pixel would be the same as the LIRs of SGR (14) for all m . For $\zeta > 0$, $\zeta \|\mathbf{T}_{\text{time}} \mathbf{f}_c\|_2^2$ term in (25) encourages each LIR of the m th frame to be the same as one another, which can result in different spatial resolution for different ζ .

E. Local Impulse Response (LIR) Summary

The main results of this section are the LIR expressions (16), (22), and (27) for the PMC, PMM, and MTR methods for MCIR, respectively. Readers familiar with [21] will recognize that these LIR expressions reflect nonuniform and anisotropic spatial resolution, both due to heteroscedastic noise and due to nonrigid motion for standard regularizers. Section IV presents regularization design methods that can provide approximately uniform and isotropic spatial resolution.

IV. SPATIAL REGULARIZER DESIGNS FOR MCIR

In this section, we present ways to design spatial regularizers of MCIR methods to provide approximately uniform and isotropic spatial resolution that does not depend on object-specific measurement statistics and given object-specific nonrigid motion. We extend the so-called *analytical approach* for regularizer design [29] to MCIR cases.

For the analysis in this section, we focus on 2-D PET. We consider an ideal tomography system, i.e., we ignore detector blur; nevertheless, we conjecture that the regularization designs are also useful in the presence of detector blur. We assume that

$$\mathbf{A}_m = \mathbf{D}_m \mathbf{A}_0, \quad m = 1, \dots, M \quad (29)$$

where \mathbf{D}_m denotes a diagonal matrix for patient-dependent attenuation and detector efficiency for the m th frame, and \mathbf{A}_0 is a system geometry. We assume known and well-aligned attenuation map (i.e., \mathbf{D}_m is given), which can be the case for PET-CT [38] or PET-MR [39]. We still allow the warp $\mathbf{T}_{m,1}$ to differ for each m .

For nonrigid motion, we assume that given nonrigid motion is locally affine [40]. This can be viewed as a first-order Taylor expansion of general nonrigid motion, which can be a good approximation locally for smooth motion. We limit our analysis to 2-D cases and focus on using a first-order difference matrix as a spatial regularizer.

A. Single Gated Reconstruction (SGR)

We first briefly review the ‘‘conventional’’ analytical approach for designing a regularizer that provides approximately uniform and isotropic spatial resolution for *static* image reconstruction [27], [29]. This SGR method is also suitable when reconstructing an individual frame, e.g., \mathbf{f}_m , from the corresponding measurement \mathbf{y}_m . However, the empirical results in Section V show that this conventional regularizer does not provide the intended spatial resolution for any of the MCIR methods described previously, so we provide new regularization designs for MCIR methods in subsequent subsections.

We focus on quadratic regularization methods using first-order finite differences as follows:

$$\begin{aligned} \mathbf{f}'_m \mathbf{R}_m \mathbf{f}_m &= \|\mathbf{C}_m \mathbf{f}_m\|^2 \\ &\triangleq \sum_j \sum_{l=1}^L r_{l,m}^j ((c_l * \mathbf{f}_m)[\vec{n}_j])^2 \end{aligned} \quad (30)$$

where $**$ denotes 2-D convolution, $f_m[\vec{n}_j]$ denotes the 2-D array corresponding to the lexicographically ordered vector \mathbf{f}_m , j is the lexicographic index of the pixel at \vec{n}_j and

$$c_l[\vec{n}_j] = \frac{1}{\|\vec{m}_l\|_2} (\delta_2[\vec{n}_j] - \delta_2[\vec{n}_j - \vec{m}_l]) \quad (31)$$

where $\{\vec{m}_l\}$ denote the spatial offsets of the j th pixel’s neighbors and $\delta_2[\vec{n}_j]$ denotes the 2-D Kronecker impulse. For our empirical results, we used the usual 8-pixel 2-D neighborhood with $\{\vec{m}_l\} = \{(1, 0), (0, 1), (1, 1), (1, -1)\}$.

For the single-frame estimator $\mathbf{f}_m(\mathbf{y}_m)$ in (12) with (29), one can rewrite the LIR (14) for SGR as

$$\mathbf{l}_m^j \approx [\mathbf{F}_m + \eta \mathbf{R}_m]^{-1} \mathbf{F}_m \mathbf{e}_j \quad (32)$$

where $\mathbf{F}_m \triangleq \mathbf{A}'_0 \tilde{\mathbf{W}}_m \mathbf{A}_0$ and $\tilde{\mathbf{W}}_m \triangleq \mathbf{D}'_m \mathbf{W}_m \mathbf{D}_m$ is a diagonal matrix. We would like to design the regularizer \mathbf{R}_m [i.e., to select $\{r_{l,m}^j\}$ in (30)] so that the LIR closely matches some target point spread function (PSF). A reasonable target for the j th pixel is

$$\mathbf{l}_0^j = [\mathbf{A}'_0 \mathbf{A}_0 + \eta \mathbf{R}_0]^{-1} \mathbf{A}'_0 \mathbf{A}_0 \mathbf{e}_j \quad (33)$$

which is the (often shift-invariant) LIR of a penalized unweighted least square (PULS) estimator, and \mathbf{R}_0 denotes the Hessian of a standard shift-invariant quadratic regularizer. If we assume slowly varying weights in $\tilde{\mathbf{W}}_m$ at the j th pixel, then

$\mathbf{A}'_0 \tilde{\mathbf{W}}_m \mathbf{A}_0$ becomes approximately a locally circulant matrix. One can show that ‘‘ $\mathbf{l}_m^j \approx \mathbf{l}_0^j$ ’’ approximately reduces to

$$\mathbf{R}_0 \mathbf{A}'_0 \tilde{\mathbf{W}}_m \mathbf{A}_0 \mathbf{e}_j \approx \mathbf{R}_m \mathbf{A}'_0 \mathbf{A}_0 \mathbf{e}_j. \quad (34)$$

Therefore, our regularization design becomes an optimization problem with respect to \mathbf{R}_m (or $\{r_{l,m}^j\}$) for all j and m

$$\operatorname{argmin}_{\{r_{l,m}^j\}_{l=1}^L \geq 0} \left\| \mathbf{R}_0 \mathbf{A}'_0 \tilde{\mathbf{W}}_m \mathbf{A}_0 \mathbf{e}_j - \mathbf{R}_m \mathbf{A}'_0 \mathbf{A}_0 \mathbf{e}_j \right\|_2^2 \quad (35)$$

where \mathbf{R}_m is the function of $\{r_{l,m}^j\}$ for all l and j as given in (30).

An analytical formulation can simplify (35) by using a frequency domain representation. For polar coordinates (ρ, φ) in frequency space, we write $\mathbf{A}'_0 \mathbf{A}_0 \equiv |B(\rho)|^2 / \rho$ to indicate that $\mathbf{A}'_0 \mathbf{A}_0$ is a locally shift-invariant operator with local frequency response $|B(\rho)|^2 / \rho$ where $B(\cdot)$ denotes the frequency response of a typical radial blur function $b(r)$ (e.g., the blur at the center of a single projection view). For a standard quadratic penalty function \mathbf{R}_0 (i.e., $\int \|\nabla f_m\|^2$), one can show that $\mathbf{R}_0 \equiv (2\pi\rho)^2$, and the quadratic function (30) becomes $\mathbf{R}_m \equiv \sum_{l=1}^L r_{l,m}^j (2\pi\rho)^2 \cos^2(\varphi - \varphi_l)$, where $\varphi_l = \angle \vec{m}_l$. One can also show by using the Fourier slice theorem and assuming the local shift invariance of $\mathbf{A}'_0 \tilde{\mathbf{W}}_m \mathbf{A}_0$ (slowly varying $\tilde{\mathbf{W}}_m$) that [41]

$$\mathbf{F}_m = \mathbf{A}'_0 \tilde{\mathbf{W}}_m \mathbf{A}_0 \equiv \frac{\bar{w}_m(\varphi; \vec{x}_j) |B_\varphi^j(\rho)|^2}{\rho} \quad (36)$$

where $B_\varphi^j(\cdot)$ denotes the (local) frequency response of the detector response $b_\varphi^j(r)$ at angle φ local to where the j th pixel projects onto the detector at that angle, and the angular-dependent weighting $\bar{w}_m(\varphi; \vec{x}_j)$ for the j th pixel is

$$\bar{w}_m(\varphi; \vec{x}_j) \triangleq \frac{\sum_{i \in \mathcal{I}_\varphi} a_{ij}^2 \tilde{w}_{m,i}}{\sum_{i \in \mathcal{I}_\varphi} a_{ij}^2} \quad (37)$$

where \mathcal{I}_φ is the set of rays at the angle φ , $a_{ij} \triangleq [\mathbf{A}_0]_{ij}$, and $\tilde{w}_{m,i} \triangleq [\tilde{\mathbf{W}}_m]_{ii}$. We simplify (35) to the following cost function with respect to $\{r_{l,m}^j\}$ for each m and j

$$\operatorname{argmin}_{\{r_{l,m}^j\}_{l=1}^L \geq 0} \Psi \left(r_{l,m}^j, \bar{w}_m(\varphi; \vec{x}_j) \right) \quad (38)$$

where

$$\Psi \left(r_{l,m}^j, w \right) \triangleq \int_0^\pi \left[w - \sum_{l=1}^L r_{l,m}^j \cos^2(\varphi - \varphi_l) \right]^2 d\varphi. \quad (39)$$

We can solve (38) analytically using Karush–Kuhn–Tucker conditions or iteratively using an iterative nonnegative least squares method. This summarizes [27], [29] for static 2-D imaging. We extend these methods to MCIR next.

B. Postreconstruction Motion Correction (PMC)

We would like to design regularizers \mathbf{R}_m that can approximate $\mathbf{l}_{\text{PMC}}^j \approx \mathbf{l}_0^j$ for all j . Equations (16) and (33) show that if we design a regularizer \mathbf{R}_m such that

$$[\mathring{\mathbf{F}}_m + \eta \mathring{\mathbf{R}}_m]^{-1} \mathring{\mathbf{F}}_m \mathbf{e}_j \approx [\mathbf{F}_0 + \eta \mathbf{R}_0]^{-1} \mathbf{F}_0 \mathbf{e}_j \quad (40)$$

for all m where $\mathbf{F}_0 \triangleq \mathbf{A}'_0 \mathbf{A}_0$, then we can achieve $\mathbf{U}_{\text{PMC}}^j \approx \mathbf{U}_0^j$. Equivalently, we want to design \mathbf{R}_m (or $r_{l,m}^j$) such that

$$[\mathbf{F}_m + \eta \mathbf{R}_m]^{-1} \mathbf{F}_m \mathbf{e}_j \approx \mathring{\mathbf{T}}_{m,1} [\mathbf{F}_0 + \eta \mathbf{R}_0]^{-1} \mathbf{F}_0 \mathring{\mathbf{T}}_{1,m} \mathbf{e}_j \quad (41)$$

for all m . For small η , $[\mathbf{F}_0 + \eta \mathbf{R}_0]^{-1} \mathbf{F}_0$ will be approximately diagonal, so by (7) and (8), we can cancel the diagonal matrices in $\mathring{\mathbf{T}}_{m,1}$ and $\mathring{\mathbf{T}}_{1,m}$ so that (41) becomes

$$[\mathbf{F}_m + \eta \mathbf{R}_m]^{-1} \mathbf{F}_m \mathbf{e}_j \approx \mathbf{T}_{m,1} [\mathbf{F}_0 + \eta \mathbf{R}_0]^{-1} \mathbf{F}_0 \mathbf{T}_{1,m} \mathbf{e}_j. \quad (42)$$

By assuming the warp is locally affine and $\mathring{\mathbf{T}}_{m,1} \mathbf{F}_0 \mathring{\mathbf{T}}_{1,m}$ is approximately circulant locally, (42) becomes the following optimization problem for each m and j :

$$\operatorname{argmin}_{\{r_{l,m}^j\}_{l=1}^L \geq 0} \|\mathbf{T}_{m,1} \mathbf{R}_0 \mathbf{T}_{1,m} \mathbf{F}_m \mathbf{e}_j - \mathbf{R}_m \mathbf{T}_{m,1} \mathbf{F}_0 \mathbf{T}_{1,m} \mathbf{e}_j\|_2. \quad (43)$$

We need to determine an analytical form for $\mathbf{T}_{m,1} \mathbf{R}_0 \mathbf{T}_{1,m}$ and $\mathbf{T}_{m,1} \mathbf{F}_0 \mathbf{T}_{1,m}$ to solve (43) efficiently. With the results of Appendices A and B (assuming locally affine transforms $\mathbf{T}_{m,1}$ and $\mathbf{T}_{1,m}$), one can show the equivalent continuous forms of $\mathbf{T}_{m,1} \mathbf{F}_0 \mathbf{T}_{1,m}$ and $\mathbf{T}_{m,1} \mathbf{R}_0 \mathbf{T}_{1,m}$ at the j th pixel are as follows:

$$\mathbf{T}_{m,1} \mathbf{F}_0 \mathbf{T}_{1,m} \equiv \frac{|B(\rho)|^2}{\rho \|\nabla T_{1,m}(\vec{x}_j)'(\cos \varphi, \sin \varphi)'\|_2} \quad (44)$$

$$\mathbf{T}_{m,1} \mathbf{R}_0 \mathbf{T}_{1,m} \equiv (2\pi\rho)^2 \|\nabla T_{1,m}(\vec{x}_j)'(\cos \varphi, \sin \varphi)'\|_2^2 \quad (45)$$

where we ignore detector blur (i.e., $b(r) \approx \delta(r)$ or $B(\rho) \approx 1$) in (45). Thus, using a procedure similar to Section IV-A, we perform (43) by minimizing the following cost function with respect to $\{r_{l,m}^j\}$ for each m and j

$$\operatorname{argmin}_{\{r_{l,m}^j\}_{l=1}^L \geq 0} \Psi(r_{l,m}^j, \bar{w}_{\text{PMC},m}(\varphi; \vec{x}_j)) \quad (46)$$

where the angular-dependent weighting for the j th pixel is

$$\bar{w}_{\text{PMC},m}(\varphi; \vec{x}_j) \triangleq \bar{w}_m(\varphi; \vec{x}_j) \|\nabla T_{1,m}(\vec{x}_j)'(\cos \varphi, \sin \varphi)'\|_2^3$$

and $\bar{w}_m(\varphi; \vec{x}_j)$ is defined in (37). $\bar{w}_m(\varphi; \vec{x}_j)$ describes the nonuniformity and anisotropy of the spatial resolution due to the interaction between the likelihood and the regularizer, which is also observed in (38) for SGR. $\|\nabla T_{1,m}(\vec{x}_j)'(\cos \varphi, \sin \varphi)'\|_2^3$ is an additional term to explain the nonuniformity and anisotropy due to motion. As mentioned in Section IV-A, one can solve optimization problems of the form (46) analytically or iteratively [27], [29].

C. Parametric Motion Model (PMM)

For uniform and isotropic spatial resolution, we would like to design \mathbf{R}_{PMM} (which is of the form (30) with r_l^j) to satisfy $\mathbf{U}_{\text{PMM}}^j \approx \mathbf{U}_0^j$ from (22) and (33). By assuming a locally affine transform, \mathbf{F}_m in (22) will be a locally circulant matrix at the

j th voxel, which reduces $\mathbf{U}_{\text{PMM}}^j \approx \mathbf{U}_0^j$ to the following simpler optimization problem:

$$\operatorname{argmin}_{\{r_l^j\}_{l=1}^L \geq 0} \left\| \mathbf{R}_0 \sum_{m=1}^M \mathring{\mathbf{F}}_m \mathbf{e}_j - \mathbf{R}_{\text{PMM}} \mathbf{F}_0 \mathbf{e}_j \right\|_2 \quad (47)$$

for all j . Ignoring detector blur, one can use Appendix B to show that the analytical form for $\mathring{\mathbf{F}}_m$ is

$$\mathring{\mathbf{F}}_m \equiv \frac{\bar{w}_m(\tilde{\varphi}; T_{m,1}^{-1}(\vec{x}_j)) |\nabla T_{m,1}(\vec{x}_j)'|^{2p-1}}{\rho \|\nabla T_{m,1}(\vec{x}_j)'(\cos \varphi, \sin \varphi)'\|_2} \quad (48)$$

where $\tilde{\varphi} \triangleq \angle \nabla T_{m,1}(\vec{x}_j)'(\cos \varphi, \sin \varphi)'$. With a similar procedure as in Section IV-A, one can reduce (47) to minimizing the following cost function with respect to r_l^j of \mathbf{R}_{PMM} :

$$\operatorname{argmin}_{\{r_l^j\}_{l=1}^L \geq 0} \Psi(r_l^j, \bar{w}_{\text{PMM}}(\varphi; \vec{x}_j)) \quad (49)$$

for all j where Ψ was defined in (39) and

$$\bar{w}_{\text{PMM}}(\varphi; \vec{x}_j) = \sum_{m=1}^M \frac{|\nabla T_{m,1}(\vec{x}_j)'|^{2p-1} \bar{w}_m(\tilde{\varphi}; T_{m,1}^{-1}(\vec{x}_j))}{\|\nabla T_{m,1}(\vec{x}_j)'(\cos \varphi, \sin \varphi)'\|_2}$$

The term $\bar{w}_m(\tilde{\varphi}; T_{m,1}^{-1}(\vec{x}_j))$ accounts for displacement of the activity due to motion and the term $|\nabla T_{m,1}(\vec{x}_j)'|^{2p-1} / \|\nabla T_{m,1}(\vec{x}_j)'(\cos \varphi, \sin \varphi)'\|_2$ accounts for activity changes due to local volume change. Unlike PMC, for PMM, the nonuniformity and anisotropy of spatial resolution due to motion and due to the interaction between likelihood and regularizer are closely related. Note that the nonuniformity and anisotropy of the spatial resolution due to motion can be more severe when the warp is not total activity-preserving (i.e., $p = 0$). One can solve the optimization problem (49) analytically or iteratively [27].

D. Motion-Compensated Temporal Regularization (MTR)

For MTR, we would like to design \mathbf{R}_m for all m to achieve

$$\mathbf{U}_{\text{MTR}}^j \approx [(\mathbf{U}_0^j)', (\mathbf{T}_{2,1} \mathbf{U}_0^j)', \dots, (\mathbf{T}_{M,1} \mathbf{U}_0^j)']' \quad (50)$$

which means that we want to approximately match the LIR of the “first” frame at the j th pixel to \mathbf{U}_0^j and the LIRs of other frames should satisfy the given motion relationships related to the first frame.

We can simplify the design problem (50) as follows. For $\zeta = 0$ in (25), (50) is equivalent to (41) for all m . In Section IV-B, we designed the regularizer (46) for each frame m to approximately match the spatial resolution to the PULS estimator (uniform and isotropic), i.e., satisfying (41). After we design \mathbf{R}_m for all m using (46), then the $\zeta \|\mathbf{T}_{\text{time}} \mathbf{f}_c\|_2^2$ term in (25) is approximately zero due to the transitivity (11). Therefore, as we increase $\zeta > 0$, we can still satisfy (50) with the regularizers \mathbf{R}_m from (46) without affecting the cost function in (25). The temporal regularizer only increases the correlation between image frames and $\zeta \mathbf{R}_{\text{time}}$ does not affect the LIR of all frames in MTR under the assumption (40). Therefore, we can approximately

match the spatial resolution of MTR with our target spatial resolution of PULS estimator using the proposed PMC regularizer design (46).

V. SIMULATION RESULTS

The general analyses provided in the previous section apply to nonrigid motions that are approximately locally affine. We performed two simulations with digital phantoms: one is a simple phantom with global affine motion between frames and the other is a XCAT phantom [42] with general nonrigid motion that is modeled using B-splines [35].

A. Simulation Setting

We used two digital phantoms, each with four frames of 160×160 pixels with 3.4 mm pixel width. We forward-projected these original images using a PET scanner geometry with 240 detector samples, 3.4 mm spacing, 220 angular views, and 3.4 mm strip width. We used 400 K, 200 K, 300 K, 300 K mean true coincidences for each frame (1.2 M total) with 10% random coincidences. We used simple uniform attenuation maps for the first simulation and ignored attenuation for the second simulation. We scaled the image intensities to preserve the total activity as described in Section II-C.

We investigated various reconstruction methods as follows. Target refers to a PULS estimator (33) that shows our target spatial resolution with $\eta = 10^4$. SGR-S refers to a standard gated (single frame) reconstruction method (12). PMC-S, PMC-C, and PMC-P refer to PMC estimation results using a conventional static regularizer, a certainty-based regularizer [21], and our proposed regularizer designed using (46), respectively. PMM-S, PMM-C, and PMM-P also refer to PMM reconstructed images using a conventional static regularizer, a certainty-based spatial regularizer, and our proposed regularizer from (49) respectively. Lastly, MTR-S and MTR-P refers to MTR results using a conventional static regularizer and our proposed spatial regularizer (46) respectively. PMC and PMM were reconstructed using a regularized expectation-maximization (EM) algorithm with Poisson likelihood [43]. PULS and MTR were reconstructed by using preconditioned conjugate gradient with PWLS for simplicity.

B. Simple Phantom With Affine Motion

In this simulation, we used a simple digital phantom with known affine motion (anisotropic scaling between frame 1 and 2, rotation between frame 2 and 3, and translation between frame 3 and 4) as shown in Fig. 2.

We put an impulse at (101,61) and generated two noiseless projections with original and impulse-added images. We obtained LIRs by subtracting a reconstructed original image from a reconstructed impulse-added image as defined in (13). Figs. 3 and 4 show contour plots of the LIRs of the different MCIR methods and different regularization schemes. Using static spatial regularizers usually led to skewed LIRs (for PMC-S, PMM-S, and MTR-S) due to the spatial-variant noise statistics and the motion. Certainty-based spatial regularizer designs did not alleviate the skewness of LIRs for each MCIR method (PMC-C and PMM-C) and the LIRs of PMC-C and PMM-C do not match the target well. However, our proposed spatial

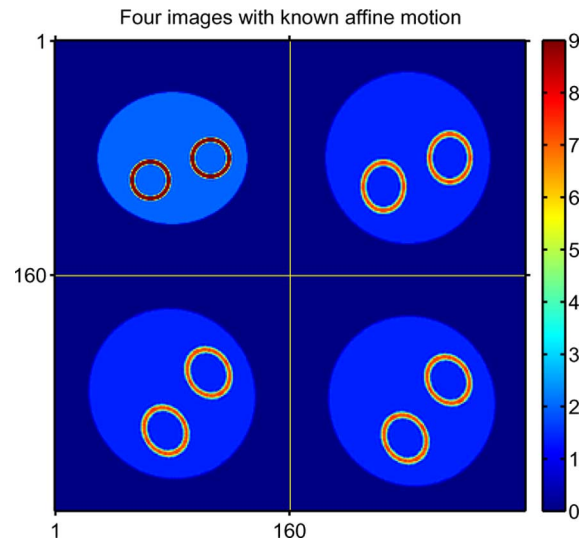


Fig. 2. Four true images with anisotropic scale, rotation and translation.

regularization designs of (46) and (49) achieve approximately uniform and isotropic spatial resolution that matches well with our target resolution (PULS estimator) for each MCIR method (PMC-P, PMM-P, and MTR-P with a wide range of ζ). With the proposed regularizer designs, PMC, MTR, and PMM can have approximately the same spatial resolution.

The skewed LIRs for conventional regularizers can cause nonuniform estimation bias in small or narrow structures such as small lesions or rings as shown in Fig. 5. These mean images were obtained from the noiseless projections [22]. Fig. 5(a) shows profiles of the relative image intensity around the right ring of the PMC reconstructed images. Our proposed PMC-P is very close to the target compared to the other regularization methods (PMC-S and PMC-C). The profile of Fig. 5(b) shows that our proposed regularizer obtained approximately the same quantitative result as that of the target for PMM. Fig. 5(c) shows that our proposed spatial regularizer (46) approximately achieved the same spatial resolution regardless of ζ , while the spatial resolution of MTR-S changes over ζ .

We obtained the LIRs and the mean images of different MCIR methods by reconstructing images from noiseless projection data. We also performed 100 noise realizations (regularizer were obtained from each realization) and showed that (result not shown in here) the image from one noiseless projection and the mean image from 100 noise realizations matched very well. They confirm that we can also use the same *plug-in* technique for MCIR method as that for static case [22] to predict spatial resolution properties.

C. XCAT Phantom With Nonrigid Motion

In this simulation, we used XCAT digital phantom [42] with respiratory and cardiac motion to generate four volumes with nonrigid motion and selected one slice per each volume (same location) for the 2-D simulation. We estimated the motion fields from frame 1 to 2, from frame 1 to 3, and from frame 1 to 4 (for PMM) by using B-spline nonrigid motion estimation [35] and used them as the true motion, leading to the images f_1, \dots, f_4 shown in Fig. 6. Then, we obtained the other related warps

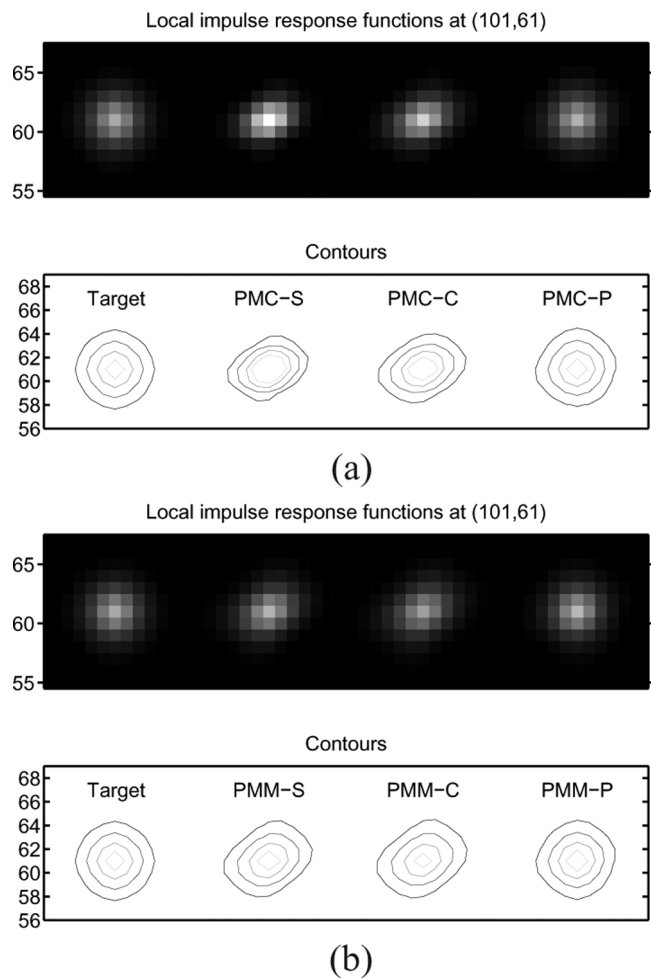


Fig. 3. LIRs (images and contours) at pixel (101, 61) for different MCIR methods. Our proposed spatial regularization designs can match well with the uniform and isotropic target LIR. (a) PMC. (b) PMM.

(e.g., motion from frame 4 to 1 for PMC and from 3 to 4 for MTR) by using (54) and the composition of transformations (e.g., $\hat{T}_{4,3} = \hat{T}_{4,1}\hat{T}_{1,3}$). Thus, there is no motion model mismatch in this experiment, so that we can focus on the spatial resolution properties.

To measure LIRs, we put nine impulses as indicated in Fig. 6 (+ marks). Fig. 7 shows the LIRs of PMC at the nine locations. Fig. 7(a) and (b) shows that conventional and certainty-based spatial regularizers lead to skewed LIRs as compared to the Target LIR. However, our proposed regularizer for PMC yielded a good match to the Target LIR as shown in Fig. 7(c). Fig. 7(d) and (e) confirms that regularizers that do not strive for isotropic spatial resolution lead to skewed LIRs as compared to the Target LIR. However, our proposed regularizer for PMM shows a good match to the Target LIR as shown in Fig. 7(f). Fig. 8 shows LIRs of MTR at nine locations. Fig. 8(a) and (b) shows that conventional regularizer cannot achieve the matched spatial resolution to the target for any ζ value, while our proposed regularizer for MTR produced nearly uniform and isotropic LIRs as in Fig. 8(c) and (d) for a wide range of ζ values.

Fig. 9 shows absolute difference images between the mean image for each method and Target. PMC-S differs the most

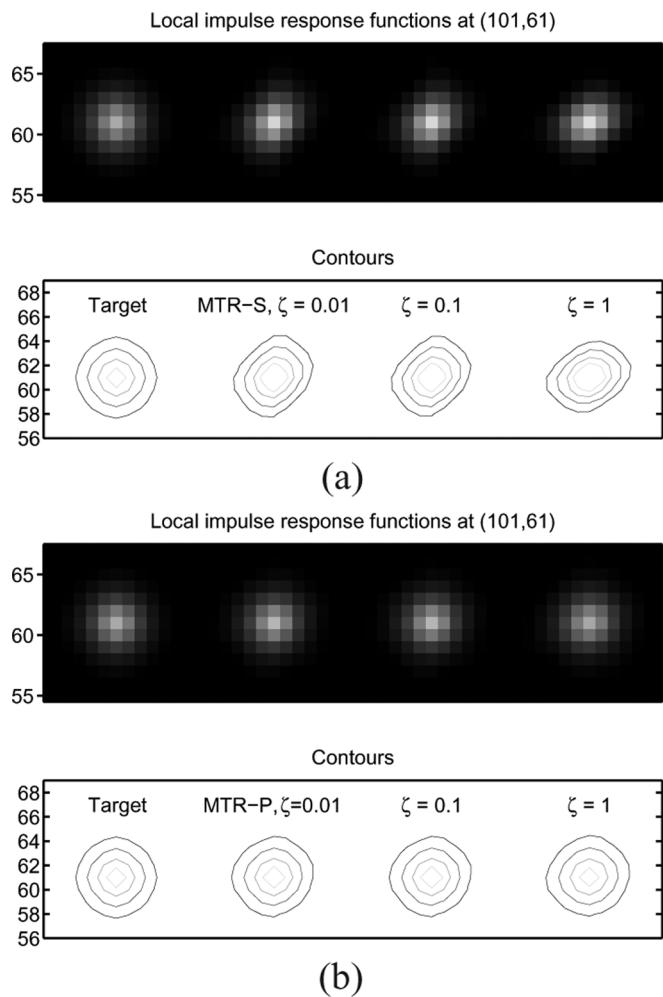


Fig. 4. LIRs (images and contours) at pixel (101, 61) for MTR. Our proposed spatial regularization designs can match well with the target LIR regardless of ζ while LIRs of MTR-S depend strongly on ζ values. (a) MTR-S. (b) MTR-P.

from the Target especially for edges and relatively small structures (near myocardium in our example) in Fig. 9(a). PMC-C matches somewhat better due to nearly uniform spatial resolution as seen in Fig. 9(b). Fig. 9(c) shows that PMC-P best matches the Target. Fig. 9(d)–(f) shows similar results for PMM. Similarly, the agreement of PMM from the Target mean image improves as the spatial regularizer encourages uniform and isotropic spatial resolution. Likewise, Fig. 10 shows that our proposed spatial regularizer for MTR yielded the mean images closest to the Target mean image for a wide range of ζ values as shown in Fig. 10(c) and (d), as compared to the results of conventional regularizers in Fig. 10(a) and (b).

VI. DISCUSSION

The analysis in this paper shows that MCIR for nonrigid (even affine) motion leads to nonuniform and anisotropic spatial resolution properties when one uses conventional static regularizers. We proposed quadratic spatial regularizers that approximately achieve isotropic and uniform spatial resolution for three different MCIR methods for the case of known non-rigid motion. Our proposed regularizers (46) and (49) yielded

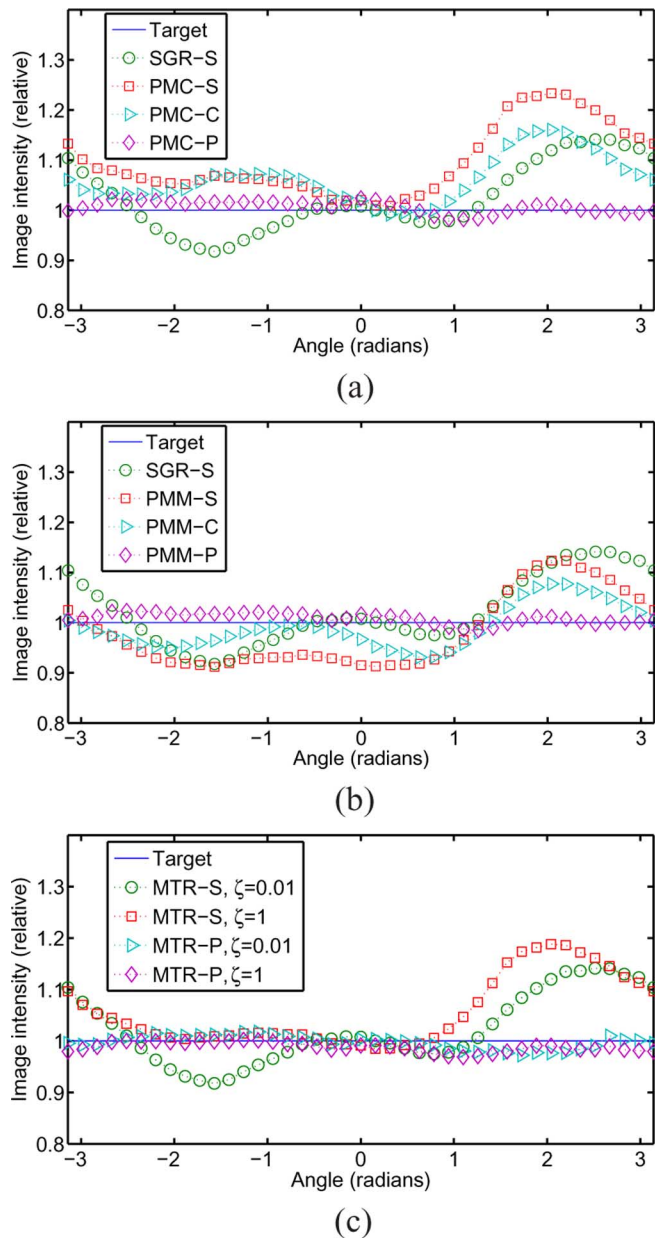


Fig. 5. Profiles around the ring on the right of reconstructed images of PMC, PMM, and MTR (with different ζ values) with different spatial regularizers from noiseless projection data. Nonuniform and/or anisotropic LIRs lead to nonuniform estimation bias in small or narrow structures such as small lesions or rings. Reconstructed images are shown in supplementary figures. (a) Ring profile of PMC. (b) Ring profile of PMM. (c) Ring profile of MTR.

LIRs that match well with the Target LIR which is isotropic and uniform.

The assumption that the motion is locally affine should be reasonable for any smooth organ motion such as heart and lungs when the time resolution is sufficient (e.g., see [44] and [45] for local affine models to approximate cardiac motion). Mathematically, the Taylor approximation of smooth nonrigid motion becomes more accurate as the region of interest (ROI) shrinks. In our analysis, the effective ROI is very small (usually about 2 pixels in each direction) because we focus on each LIR individually. Thus, even for nonaffine nonrigid motion, our proposed methods still produced LIRs that match fairly well

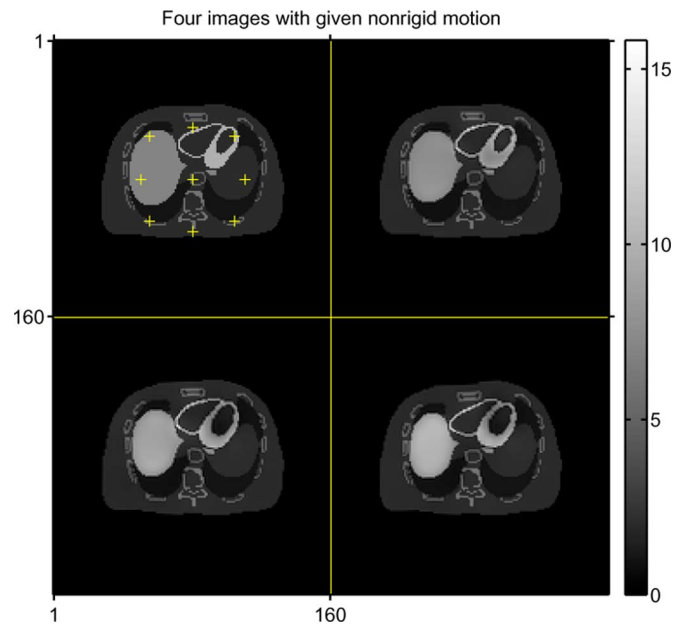


Fig. 6. Four XCAT phantom images with nonrigid motion.

with the Target LIR. However, this assumption may break for sliding motion such as the motion near the interface between diaphragm and rib cage. For lower resolution modalities like PET or SPECT, this type of motion can still be approximated by smooth motion. For high resolution imaging modalities, treating this sharp sliding motion should be further investigated along with nonquadratic spatial regularizers.

Our analysis assumed “known true motion”, but obtaining exact motion from multimodal imaging systems is challenging due to misregistration between two imaging modalities (e.g., PET and CT) and the nonlinear, nonconvex nature of image registration problem. We investigated the effect of motion error in our reconstructed images. We reconstructed the simple phantom in Section V-B again, but with 1.7 mm (a half pixel) and 3.4 mm (1 pixel) motion errors in the x-direction deformation. Additionally, we reconstructed PULS image with motion errors by minimizing $\|\mathbf{y}_c - \mathbf{A}_d \mathbf{T}_c \mathbf{f}_1\|_2^2 + \eta \|\mathbf{C}_0 \mathbf{f}_1\|_2^2$ with respect to \mathbf{f}_1 where \mathbf{C}_0 is a first-order finite difference matrix for a standard shift-invariant quadratic regularizer. When the motion estimation error was small (1.7 mm), the maximum absolute errors between the reconstructed image and the target image for PULS, PMC-S, and PMC-P were 0.7, 1.9, and 1.1. In this case, the nonuniformity and anisotropy of the bias due to the interaction between Poisson likelihood and regularizers was still significant. However, when the motion estimation error was large (3.4 mm), the maximum absolute errors for PULS, PMC-S, and PMC-P were 1.4, 2.2, and 1.7. The nonuniformity anisotropy of the bias due to the motion error started to become a dominating factor for large motion error. PMM also showed similar tendency. For small motion errors, our proposed regularizers can still reduce the nonuniformity and anisotropy of the bias as expected because \tilde{w}_m is slowly varying and we assumed local affine motion (i.e., smooth motion). For large motion errors, MCIR itself may fail to yield images with good quantification accuracy for *any* regularization method. There is much effort on improving the

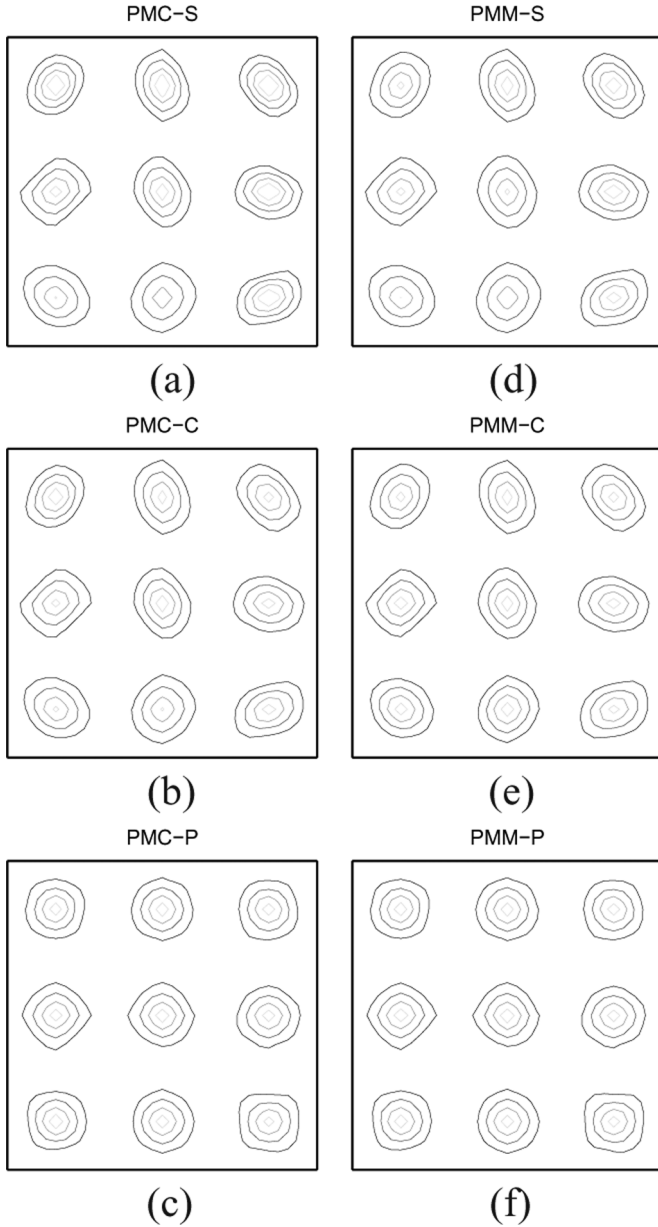


Fig. 7. Contours of LIRs for PMC and PMM. Our proposed PMC-P and PMM-P approaches approximately match with target spatial resolution for general nonrigid motion. (a) PMC-S. (b) PMC-C. (c) PMC-P. (d) PMM-S. (e) PMM-C. (f) PMM-P.

accuracy of motion estimation by using simultaneous acquisition such as PET-MR, or by using joint estimation of image and motion. The issue of the nonuniform and anisotropic spatial resolution will become increasingly important as the accuracy of the motion estimation in MCIR models continues to improve.

The spatial resolution analysis and regularizer designs in this paper can provide the basis for interesting future work such as analyzing the noise properties of MCIR methods [46] and extending regularization design to 3-D PET/CT and to nonquadratic regularizers. It is straightforward to extend this work to 3-D cylindrical PET with 6-voxel 3-D regularizer [47], which is relevant for 3-D PET rebinning methods [48]. Extending this analysis to fully 3-D PET or fan-beam CT will be more challenging, just as [23], [27] extended [21], [29],

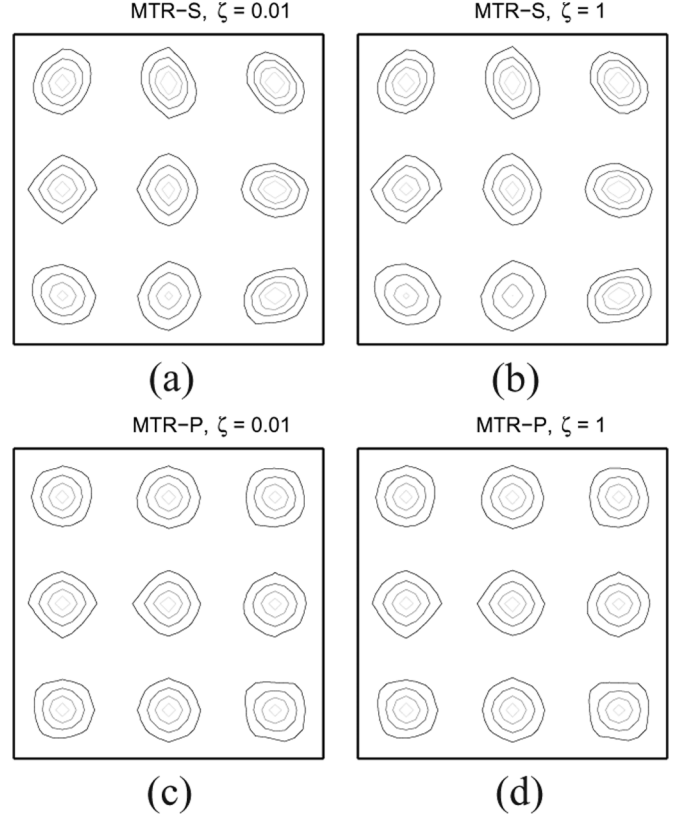


Fig. 8. Contours of LIRs for MTR. Our proposed MTR-P approximately matches with target despite general nonrigid motion and different ζ . (a) MTR-S with $\zeta = 0.01$. (b) MTR-S with $\zeta = 1$. (c) MTR-P with $\zeta = 0.01$. (d) MTR-P with $\zeta = 1$.

respectively. This analysis can also provide insights into the methods of joint image reconstruction and motion estimation (unknown motion) [7], [8], [11], [13]–[15]. One may use the proposed regularizers in the joint estimation framework by using currently estimated motion instead of using true motion. However, the effect of the proposed regularizer in this case should be further analyzed.

APPENDIX A

ADJOINT OPERATOR OF A WARP \mathcal{T}

This appendix analyzes the properties of the transpose warp matrix $\mathbf{T}'_{m,n}$ by considering its continuous space analog. Let $T : \mathbb{R}^d \rightarrow \mathbb{R}^d$ denote a spatial transformation with positive Jacobian determinant. Let $\mathcal{X} = L_2(\mathbb{R}^d)$ denote the space of (square integrable) images over \mathbb{R}^d and define the warp operator $\mathcal{T} : \mathcal{X} \rightarrow \mathcal{X}$ by $g = \mathcal{T}f$ if and only if $g(\vec{x}) = f(T(\vec{x}))$ for $f, g \in \mathcal{X}$ and all $\vec{x} \in \mathbb{R}^d$. This appendix determines the adjoint of \mathcal{T} , defined as the operator \mathcal{T}' that satisfies $\langle g, \mathcal{T}f \rangle = \langle \mathcal{T}'g, f \rangle$ for all $f, g \in \mathcal{X}$, where $\langle \cdot, \cdot \rangle$ denotes the usual inner product on \mathcal{X} .

By a simple change of variable $\vec{y} = T(\vec{x})$, we have

$$\begin{aligned} \langle g, \mathcal{T}f \rangle &= \int g(\vec{x})(\mathcal{T}f)(\vec{x})d\vec{x} = \int g(\vec{x})f(T(\vec{x}))d\vec{x} \\ &= \int f(\vec{y})\frac{1}{|\nabla T(T^{-1}(\vec{y}))|}g(T^{-1}(\vec{y}))d\vec{y} \quad (51) \end{aligned}$$

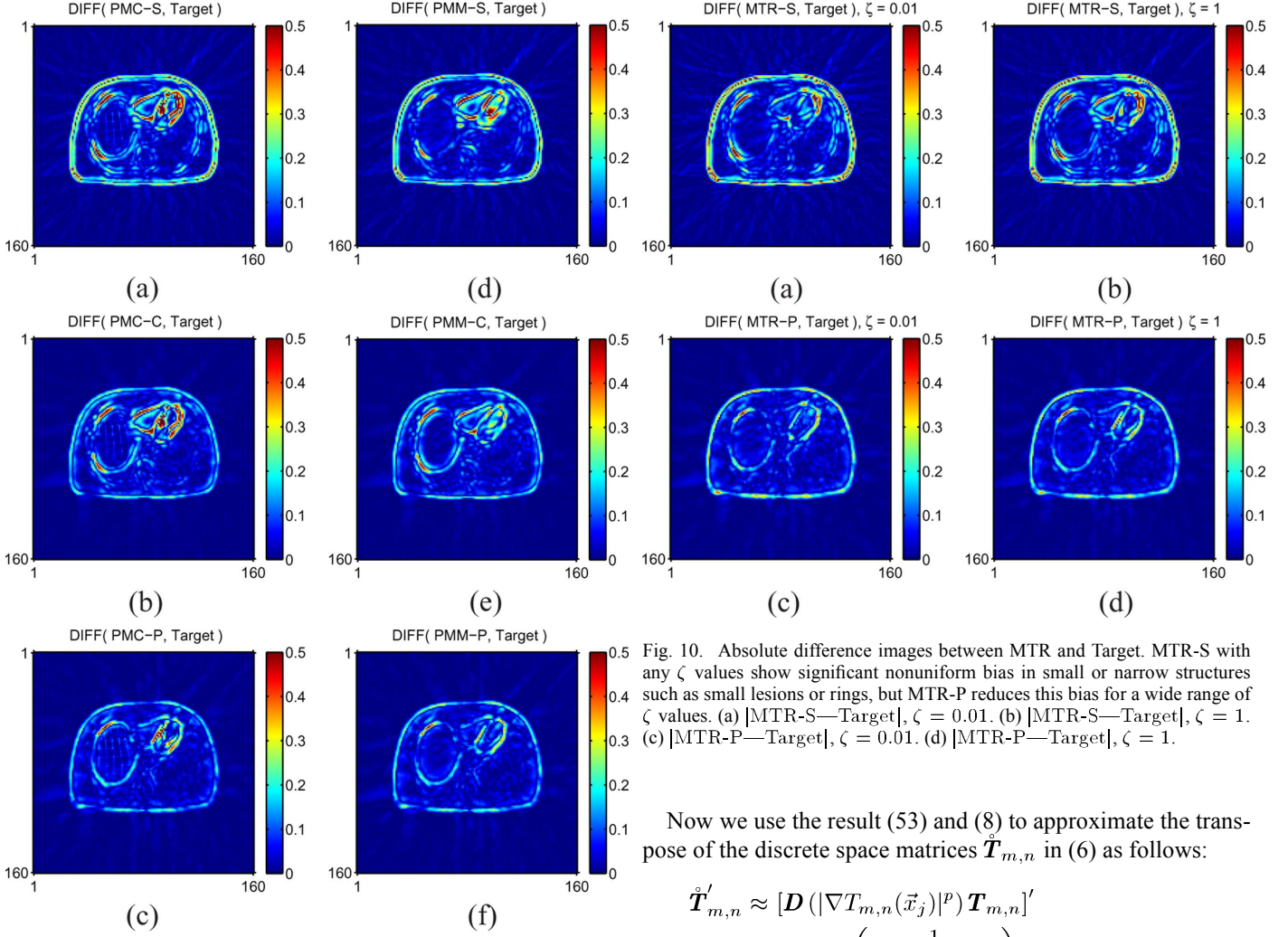


Fig. 9. Absolute difference images between PMC/PMM and target. PMC-S/PMM-S show severe nonuniform bias near edges or relatively small structures. PMC-C/PMM-C alleviate this bias using nearly uniform spatial resolution and PMC-P/PMM-P performed best by nearly uniform/isotropic spatial resolution. (a) |PMC-S—Target| (b) |PMC-C—Target| (c) |PMC-P—Target| (d) |PMM-S—Target| (e) |PMM-C—Target| (f) |PMM-P—Target|.

where $|\nabla T(\cdot)|$ denotes the determinant of Jacobian of T . We define an operator $\mathcal{D}_T : \mathcal{X} \rightarrow \mathcal{X}$ such that

$$g = \mathcal{D}_T f \quad \text{iff} \quad g(\vec{x}) = \frac{1}{|\nabla T(\vec{x})|} f(\vec{x}), \forall \vec{x}.$$

Then, by (51), the adjoint operator \mathcal{T}' is given by

$$\mathcal{T}' = \mathcal{T}^{-1} \mathcal{D}_T. \quad (52)$$

Therefore, in continuous space, the adjoint of an invertible non-rigid warp is the product of the inverse of the warp with a diagonal operator based on the local Jacobian determinant of the warp. The discrete approximation that matches (52) is

$$\mathbf{T}'_{m,n} \approx \mathbf{T}_{m,n}^{-1} \mathbf{D} \left(\frac{1}{|\nabla T_{m,n}(\vec{x}_j)|} \right). \quad (53)$$

Fig. 10. Absolute difference images between MTR and Target. MTR-S with any ζ values show significant nonuniform bias in small or narrow structures such as small lesions or rings, but MTR-P reduces this bias for a wide range of ζ values. (a) |MTR-S—Target|, $\zeta = 0.01$. (b) |MTR-S—Target|, $\zeta = 1$. (c) |MTR-P—Target|, $\zeta = 0.01$. (d) |MTR-P—Target|, $\zeta = 1$.

Now we use the result (53) and (8) to approximate the transpose of the discrete space matrices $\hat{\mathbf{T}}_{m,n}$ in (6) as follows:

$$\begin{aligned} \hat{\mathbf{T}}'_{m,n} &\approx [\mathbf{D} (|\nabla T_{m,n}(\vec{x}_j)|^p) \mathbf{T}_{m,n}]' \\ &\approx \mathbf{T}_{m,n}^{-1} \mathbf{D} \left(\frac{1}{|\nabla T_{m,n}(\vec{x}_j)|} \right) \mathbf{D} (|\nabla T_{m,n}(\vec{x}_j)|^p) \\ &\approx \mathbf{T}_{n,m} \mathbf{D} (|\nabla T_{m,n}(\vec{x}_j)|^{p-1}) \\ &\approx \mathbf{D} (|\nabla T_{n,m}(\vec{x}_j)|^{1-p}) \mathbf{T}_{n,m}. \end{aligned} \quad (54)$$

APPENDIX B EQUIVALENT FREQUENCY FORM FOR AFFINE TRANSFORMATION

This appendix analyzes the behavior of a gram matrix or a quadratic regularizer that is sandwiched in between the transpose and forward affine transformation operators such as $\hat{\mathbf{F}}_m$ and $\hat{\mathbf{R}}_m$ in (16). We consider the continuous-space analogue as follows:

$$\hat{\mathcal{T}}' \mathcal{Q}' H(\vec{w}) \mathcal{Q} \hat{\mathcal{T}} \quad (55)$$

where $H(\vec{w})$ denotes the frequency response with frequency domain variables \vec{w} , \mathcal{Q} is a Fourier transform operator, and $\hat{\mathcal{T}}$ corresponds to the total activity-preserving affine transform operator that is associated with the affine transform

$$T(\vec{x}) = \mathbf{L}\vec{x} + \vec{d}. \quad (56)$$

Here, \mathbf{L} is a $d \times d$ invertible matrix, \vec{d} is a translation vector, and \vec{x} is spatial domain coordinates in \mathbb{R}^d . If $f(\vec{x})$

has Fourier transform $F(\vec{w})$, then the Fourier transform of $(\check{T}f)(\vec{x}) = |\nabla T(\vec{x})|^p f(T(\vec{x}))$ is

$$(\mathcal{Q}\check{T}f)(\vec{w}) = |\mathbf{L}'|^{p-1} e^{j2\pi\vec{w}\cdot\mathbf{L}^{-1}\vec{d}} F((\mathbf{L}^{-1})'\vec{w}).$$

After multiplying $(\mathcal{Q}Tf)(\vec{w})$ by $H(\vec{w})$ and matching a change of variables, the inverse Fourier operator \mathcal{Q}' will result in the following continuous function:

$$\int |\mathbf{L}'|^p H(\mathbf{L}'\vec{w}) F(\vec{w}) e^{j2\pi\vec{w}\cdot(\mathbf{L}\vec{x}+\vec{d})} d\vec{w}.$$

Lastly, by Appendix A, an operator \check{T}' will change $\mathbf{L}\vec{x} + \vec{d}$ into \vec{x} and multiply by $|\mathbf{L}'|^{p-1}$. Therefore, (55) simplifies to

$$\check{T}'\mathcal{Q}'H(\vec{w})\mathcal{Q}\check{T} = \mathcal{Q}'|\mathbf{L}'|^{2p-1}H(\mathbf{L}'\vec{w})\mathcal{Q}. \quad (57)$$

Note that the translation \vec{d} does not affect the equivalent frequency response (57). For example, if $H(\vec{w}) = \|\vec{w}\|^2 = \rho^2$ in the polar frequency coordinate (ρ, Φ) , the frequency response of $\check{T}'\mathcal{Q}'H(\vec{w})\mathcal{Q}\check{T}$ will be $|\mathbf{L}'|^{2p-1}\rho^2\|\mathbf{L}'\cdot(\cos\Phi, \sin\Phi)'\|^2$.

ACKNOWLEDGMENT

The authors would like to thank the anonymous reviewers for their helpful comments which improved this paper.

REFERENCES

- [1] C. J. Ritchie, J. Hsieh, M. F. Gard, J. D. Godwin, Y. Kim, and C. R. Crawford, "Predictive respiratory gating: A new method to reduce motion artifacts on CT scans," *Radiology*, vol. 190, no. 3, pp. 847–852, Mar. 1994.
- [2] S. A. Nehmeh, Y. E. Erdi, C. C. Ling, K. E. Rosenzweig, H. Schoder, S. M. Larson, H. A. Macapinlac, O. D. Squire, and J. L. Humm, "Effect of respiratory gating on quantifying PET images of lung cancer," *J. Nucl. Med.*, vol. 43, no. 7, pp. 876–881, Jul. 2002.
- [3] G. J. Klein, B. W. Reutter, and R. H. Huesman, "Non-rigid summing of gated PET via optical flow," *IEEE Trans. Nucl. Sci.*, vol. 44, no. 4, pp. 1509–1512, Aug. 1997.
- [4] M. Dawood, N. Lang, X. Jiang, and K. P. Schafers, "Lung motion correction on respiratory gated 3-D PET/CT images," *IEEE Trans. Med. Imag.*, vol. 25, no. 4, pp. 476–485, Apr. 2006.
- [5] W. Bai and M. Brady, "Regularized B-spline deformable registration for respiratory motion correction in PET images," *Phys. Med. Biol.*, vol. 54, no. 9, pp. 2719–2736, May 2009.
- [6] E. Gravier, Y. Yang, and M. Jin, "Tomographic reconstruction of dynamic cardiac image sequences," *IEEE Trans. Imag. Process.*, vol. 16, no. 4, pp. 932–942, Apr. 2007.
- [7] B. A. Mair, D. R. Gilland, and J. Sun, "Estimation of images and non-rigid deformations in gated emission CT," *IEEE Trans. Med. Imag.*, vol. 25, no. 9, pp. 1130–1144, Sep. 2006.
- [8] M. W. Jacobson and J. A. Fessler, "Joint estimation of image and deformation parameters in motion-corrected PET," in *Proc. IEEE Nucl. Sci. Symp. Med. Imag. Conf.*, 2003, vol. 5, pp. 3290–3294.
- [9] F. Qiao, T. Pan, J. W. Clark, and O. R. Mawlawi, "A motion-incorporated reconstruction method for gated PET studies," *Phys. Med. Biol.*, vol. 51, no. 15, pp. 3769–3784, Aug. 2006.
- [10] T. Li, B. Thorndyke, E. Schreibmann, Y. Yang, and L. Xing, "Model-based image reconstruction for four-dimensional PET," *Med. Phys.*, vol. 33, no. 5, pp. 1288–1298, May 2006.
- [11] K. Taguchi, Z. Sun, W. P. Segars, E. K. Fishman, and B. M. W. Tsui, "Image-domain motion compensated time resolved 4D cardiac CT," in *Proc. SPIE 6510, Med. Imag. 2007: Phys. Med. Imag.*, 2007, pp. 651016–651016.
- [12] F. Lamare, M. J. L. Carbayo, T. Cresson, G. Kontaxakis, A. Santos, C. C. LeRest, A. J. Reader, and D. Visvikis, "List-mode-based reconstruction for respiratory motion correction in PET using non-rigid body transformations," *Phys. Med. Biol.*, vol. 52, no. 17, pp. 5187–5204, Sep. 2007.
- [13] F. Odille, N. Cindea, D. Mandry, C. Pasquier, P.-A. Vuissoz, and J. Felblinger, "Generalized MRI reconstruction including elastic physiological motion and coil sensitivity encoding," *Mag. Res. Med.*, vol. 59, no. 6, pp. 1401–1411, Jun. 2008.
- [14] S. Y. Chun and J. A. Fessler, "Joint image reconstruction and nonrigid motion estimation with a simple penalty that encourages local invertibility," in *Proc. SPIE, Med. Imag. 2009: Phys. Med. Im.*, 2009, pp. 72580U–72580U.
- [15] M. Blume, A. Martinez-Möller, A. Keil, N. Navab, and M. Rafecas, "Joint reconstruction of image and motion in gated positron emission tomography," *IEEE Trans. Med. Imag.*, vol. 29, no. 11, pp. 1892–1906, Nov. 2010.
- [16] B. Guérin, S. Cho, S. Y. Chun, X. Zhu, N. M. Alpert, G. E. Fakhri, T. Reese, and C. Catana, "Nonrigid pet motion compensation in the lower abdomen using simultaneous tagged-MRI and pet imaging," *Med. Phys.*, vol. 38, no. 6, pp. 3025–3038, 2011.
- [17] M. Elad and A. Feuer, "Restoration of a single superresolution image from several blurred, noisy, and undersampled measured images," *IEEE Trans. Imag. Process.*, vol. 6, no. 12, pp. 1646–1658, Dec. 1997.
- [18] M. Ng and N. Bose, "Mathematical analysis of super-resolution methodology," *IEEE Signal Process. Mag.*, vol. 20, no. 3, pp. 62–74, May 2003.
- [19] R. Fransens, C. Strecha, and L. Van Gool, "Optical flow based super-resolution: A probabilistic approach," *Comput. Vis. Imag. Understand.*, vol. 106, no. 1, pp. 106–115, Apr. 2007.
- [20] M. Zibetti and J. Mayer, "A robust and computationally efficient simultaneous super-resolution scheme for image sequences," *IEEE Trans. Circuits Syst. Video Technol.*, vol. 17, no. 10, pp. 1288–1300, Oct. 2007.
- [21] J. A. Fessler and W. L. Rogers, "Spatial resolution properties of penalized-likelihood image reconstruction methods: Space-invariant tomographs," *IEEE Trans. Imag. Process.*, vol. 5, no. 9, pp. 1346–1358, Sep. 1996.
- [22] J. A. Fessler, "Mean and variance of implicitly defined biased estimators (such as penalized maximum likelihood): Applications to tomography," *IEEE Trans. Imag. Process.*, vol. 5, no. 3, pp. 493–506, Mar. 1996.
- [23] J. Qi and R. M. Leahy, "Resolution and noise properties of MAP reconstruction for fully 3D PET," *IEEE Trans. Med. Imag.*, vol. 19, no. 5, pp. 493–506, May 2000.
- [24] J. W. Stayman and J. A. Fessler, "Regularization for uniform spatial resolution properties in penalized-likelihood image reconstruction," *IEEE Trans. Med. Imag.*, vol. 19, no. 6, pp. 601–615, Jun. 2000.
- [25] J. Nuyts and J. A. Fessler, "A penalized-likelihood image reconstruction method for emission tomography, compared to post-smoothed maximum-likelihood with matched spatial resolution," *IEEE Trans. Med. Imag.*, vol. 22, no. 9, pp. 1042–1052, Sep. 2003.
- [26] S. Ahn and R. M. Leahy, "Analysis of resolution and noise properties of nonquadratically regularized image reconstruction methods for PET," *IEEE Trans. Med. Imag.*, vol. 27, no. 3, pp. 413–424, Mar. 2008.
- [27] H. R. Shi and J. A. Fessler, "Quadratic regularization design for 2D CT," *IEEE Trans. Med. Imag.*, vol. 28, no. 5, pp. 645–656, May 2009.
- [28] E. Asma and R. M. Leahy, "Mean and covariance properties of dynamic PET reconstructions from list-mode data," *IEEE Trans. Med. Imag.*, vol. 25, no. 1, pp. 42–54, Jan. 2006.
- [29] J. A. Fessler, "Analytical approach to regularization design for isotropic spatial resolution," in *Proc. IEEE Nucl. Sci. Symp. Med. Imag. Conf.*, 2003, vol. 3, pp. 2022–2026.
- [30] S. Y. Chun and J. A. Fessler, "Regularization design for isotropic spatial resolution in motion-compensated image reconstruction," in *Proc. IEEE Int. Symp. Biomed. Imag.*, 2011, pp. 1500–1503.
- [31] M. Unser, A. Aldroubi, and M. Eden, "B-spline signal processing: Part I—Theory," *IEEE Trans. Signal Process.*, vol. 41, no. 2, pp. 821–833, Feb. 1993.
- [32] D. Sarrut, V. Boldea, S. Miguet, and C. Ginestet, "Simulation of four-dimensional CT images from deformable registration between inhale and exhale breath-hold CT scans," *Med. Phys.*, vol. 33, no. 3, pp. 605–617, Mar. 2006.
- [33] V. Gorbunova, P. Lo, M. Loeve, H. A. Tiddens, J. Sporring, M. Nielsen, and M. de Bruijne, "Mass preserving registration for lung CT," in *Proc. Soc. Photo-Optical Instrum. Eng. (SPIE) Conf. Ser.*, Feb. 2009, vol. 7259.
- [34] E. Asma, R. Manjeshwar, and K. Thielemans, "Theoretical comparison of motion correction techniques for PET image reconstruction," in *Proc. IEEE Nucl. Sci. Symp. Med. Im. Conf.*, 2006, vol. 3, pp. 1762–1767.
- [35] S. Y. Chun and J. A. Fessler, "A simple regularizer for B-spline non-rigid image registration that encourages local invertibility," *IEEE J. Sel. Topics Signal Process.*, vol. 3, no. 1, pp. 159–169, Feb. 2009.

- [36] O. Skrinjar and H. Tagare, "Symmetric, transitive, geometric deformation and intensity variation invariant nonrigid image registration," in *Proc. Int. Symp. Biomed. Imag.: Nano to Macro*, Apr. 2004, vol. 1, pp. 920–923.
- [37] M. V. W. Zibetti, F. S. V. Bazán, and J. Mayer, "Determining the regularization parameters for super-resolution problems," *Signal Process.*, vol. 88, no. 12, pp. 2890–2901, 2008.
- [38] A. M. Alessio, P. E. Kinahan, K. M. Champley, and J. H. Caldwell, "Attenuation-emission alignment in cardiac PET/CT based on consistency conditions," *Med. Phys.*, vol. 37, no. 3, pp. 1911–1920, 2010.
- [39] M. Hofmann, B. Pichler, B. Schlkopf, and T. Beyer, "Towards quantitative PET/MRI: A review of MR-based attenuation correction techniques," *Eur. J. Nucl. Med. Molecul. Imag.*, vol. 36, pp. 93–104, 2009.
- [40] K. Taguchi and H. Kudo, "Motion compensated fan-beam reconstruction for nonrigid transformation," *IEEE Trans. Med. Imag.*, vol. 27, no. 7, pp. 907–917, Jul. 2008.
- [41] H. Shi, "Fast regularization design for tomographic image reconstruction for uniform and isotropic spatial resolution," Ph.D. dissertation, Univ. Michigan, Ann Arbor, 2008.
- [42] W. P. Segars, M. Mahesh, T. J. Beck, E. C. Frey, and B. M. W. Tsui, "Realistic CT simulation using the 4D XCAT phantom," *Med. Phys.*, vol. 35, no. 8, pp. 3800–3808, Aug. 2008.
- [43] A. R. De Pierro, "A modified expectation maximization algorithm for penalized likelihood estimation in emission tomography," *IEEE Trans. Med. Imag.*, vol. 14, no. 1, pp. 132–137, Mar. 1995.
- [44] M. Suhling, M. Arigovindan, C. Jansen, P. Hunziker, and M. Unser, "Myocardial motion analysis from b-mode echocardiograms," *IEEE Trans. Image Process.*, vol. 14, no. 4, pp. 525–536, Apr. 2005.
- [45] M. Hu, G. Penney, D. Rueckert, P. Edwards, M. Figl, P. Pratt, and D. Hawkes, "A novel algorithm for heart motion analysis based on geometric constraints," *Med. Image Comput. Computer-Assisted Intervent. (MICCAI)*, vol. 5241, pp. 720–728, 2008.
- [46] S. Y. Chun and J. A. Fessler, "Spatial resolution and noise properties of regularized motion-compensated image reconstruction," in *Proc. IEEE Int. Symp. Biomed. Imag.*, 2009, pp. 863–866.
- [47] H. Shi and J. A. Fessler, "Quadratic regularization design for 3D cylindrical PET," in *Proc. IEEE Nucl. Sci. Symp. Med. Imag. Conf.*, 2005, vol. 4, pp. 2301–2305.
- [48] M. Defrise, P. E. Kinahan, D. W. Townsend, C. Michel, M. Sibomana, and D. F. Newport, "Exact and approximate rebinning algorithms for 3-D PET data," *IEEE Trans. Med. Imag.*, vol. 16, no. 2, pp. 145–158, Apr. 1997.

Supplementary figures for “Spatial resolution properties of motion-compensated tomographic image reconstruction methods”

Se Young Chun, *Member, IEEE*, and Jeffrey A. Fessler, *Fellow, IEEE*

I. SIMULATION RESULTS

A. Simple phantom with affine motion

Fig. 1 (a) and (b) show that the image intensities around the rings are nonuniform due to the anisotropic and/or non-uniform spatial resolutions of PMC-S and PMC-C. Fig. 1 (c) shows our proposed PMC-P, which approximately achieved the same spatial resolution as the target image in Fig. 1 (d) with isotropic and uniform spatial resolution.

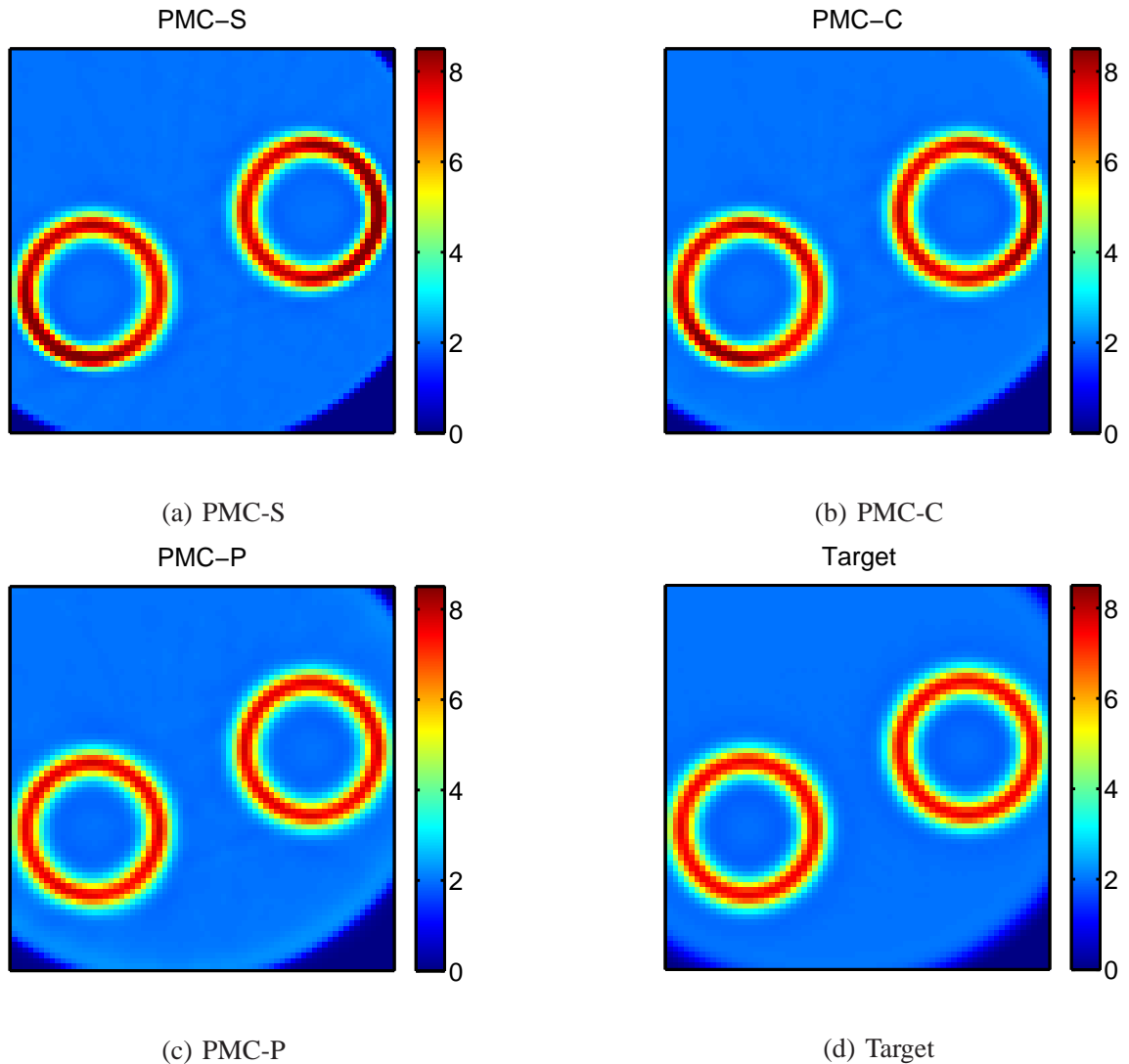


Fig. 1. Reconstructed images of PMC with different spatial regularizers from the noiseless projection data. Nonuniform and/or anisotropic LIRs lead to non-uniform estimation bias in small or narrow structures such as small lesions or rings.

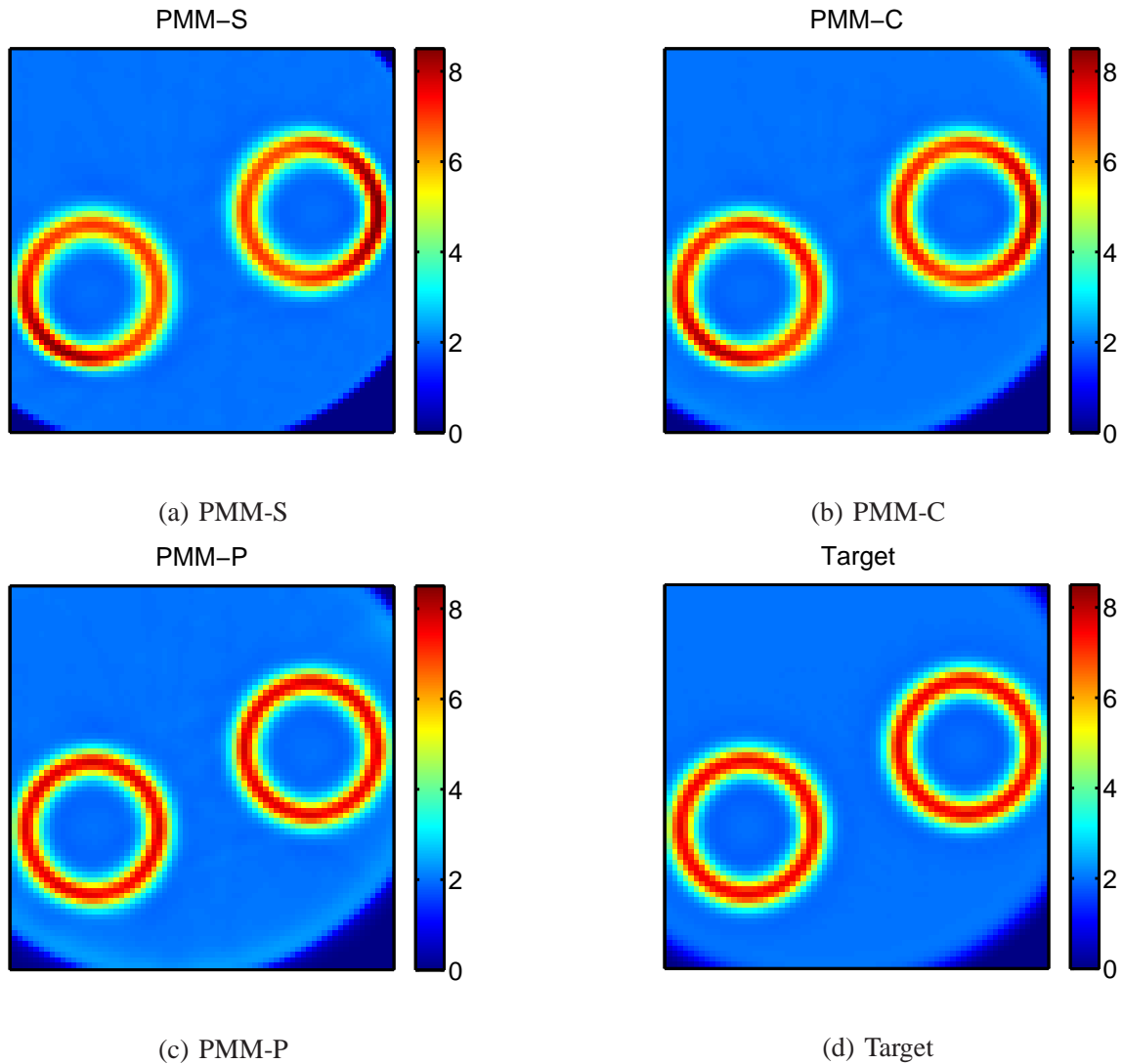


Fig. 2. Reconstructed images of PMM with different spatial regularizers from the noiseless projection data. Nonuniform and/or anisotropic LIRs lead to non-uniform estimation bias in small or narrow structures such as small lesions or rings.

Fig. 2 also shows similar results: PMM-S and PMM-C caused non-uniform estimation bias due to the spatial-variant data statistics and the motion, but PMM-P achieved approximately the same isotropic and uniform spatial resolution as those of the target PULS estimator.

Fig. 3 shows that our proposed spatial regularization method for MTR, denoted MTR-P, approximately achieved the same spatial resolution regardless of ζ , whereas the spatial resolution of MTR-S changes with ζ .

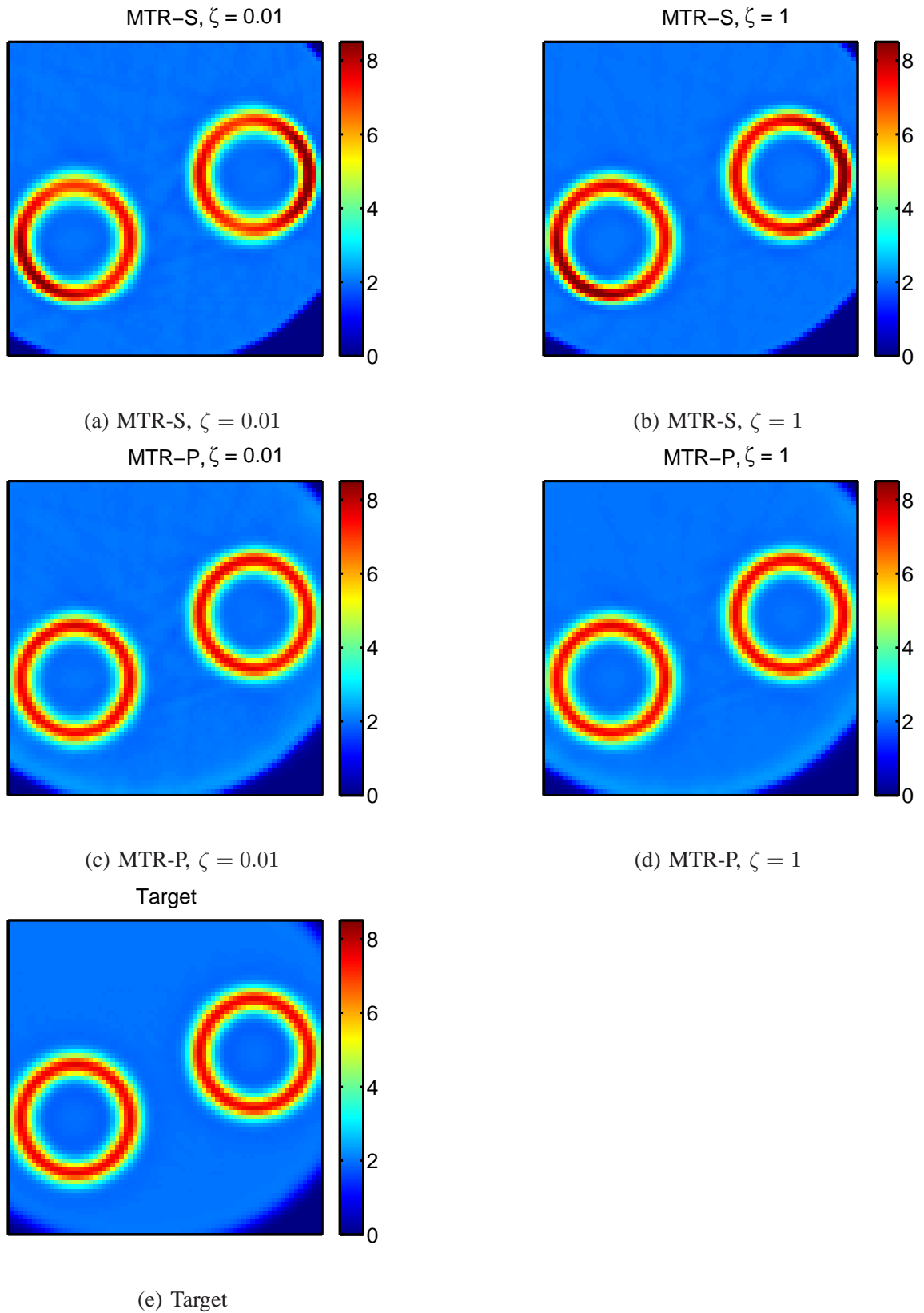


Fig. 3. Reconstructed images of MTR-S, MTR-P with different ζ values from the noiseless projection data. Nonuniform and/or anisotropic LIRs lead to non-uniform estimation bias in small or narrow structures such as small lesions or rings.